

Coupling Asymmetry Optimizes Collective Dynamics over Multiplex Networks

Zhao Song and Dane Taylor

Abstract—Networks are often interconnected, with one system wielding greater influence over another. However, the effects of such asymmetry on self-organized phenomena (e.g., consensus and synchronization) are not well understood. Here, we study collective dynamics using a generalized graph Laplacian for multiplex networks containing layers that are asymmetrically coupled. We explore the nonlinear effects of coupling asymmetry on the convergence rate toward a collective state, finding that asymmetry induces one or more optima that maximally accelerate convergence. When a faster and a slower system are coupled, depending on their relative timescales, their optimal coupling is either *cooperative* (network layers mutually depend on one another) or *non-cooperative* (one network directs another without a reciprocated influence). It is often optimal for the faster system to more-strongly influence the slower one, yet counter-intuitively, the opposite can also be true. As an application, we model collective decision-making for a human-AI system in which a social network is supported by an AI-agent network, finding that a cooperative optimum requires that these two networks operate on a sufficiently similar timescale. More broadly, our work highlights the *optimization of coupling asymmetry and timescale balancing* as fundamental concepts for the design of collective behavior over interconnected systems.

Index Terms—Multiplex Networks, Asymmetric Coupling, Interconnected Systems, SupraLaplacian, Consensus Dynamics.



1 INTRODUCTION

COLLECTIVE dynamics are widespread in nature and technology [1] with applications ranging from synchronized oscillations in brains [2] and power grids [3] to consensus processes in social networks [4]–[7], animal groups [8], [9], and decentralized algorithms for machine learning and AI [10]–[15]. The formulation of many such models involves a graph Laplacian matrix \mathbf{L} whose entries encode a network, including models for the synchronization of networks of identical dynamical systems [16], [17] and heterogeneous phase oscillators [18], [19], consensus dynamics [15], [20], Markov chains [21], [22], diffusion [23], [24], and DC electricity flow [25]. The analyses of such systems often utilize spectral theory, and in particular, the second-smallest eigenvalue λ_2 of \mathbf{L} can help determine dynamical properties such as convergence rate [15], [20] and local stability [16], [17].

One should note, however, that systems rarely exist in total isolation, and it is important to understand the dynamics of interconnected (i.e., multilayer) networks [26], [27]. A popular modeling framework is multiplex networks [28], consisting of *network layers*, each involving the same set of nodes but possibly different edges (called *intra-layer edges*). In recent years, there has been growing interest in extending Laplacian-based models to the setting of multiplex

networks, including work on random walks [29]–[32], synchronization [33]–[37], and diffusion [38]–[40]. Of particular importance are *supraLaplacian matrices* [38], [39] that generalize graph Laplacians to multiplex networks, thereby extending the general field of Laplacian-based dynamics to this setting. Importantly, existing research on supraLaplacian matrices and related applications has focused on multiplex networks in which the layers are symmetrically coupled using undirected *interlayer edges*. This is problematic since the effects of asymmetry are known to play a crucial role in shaping self-organization for network-coupled dynamical systems [41]–[47], and they provide opportunities for system optimization [48]. Moreover, it is natural to assume that the relationship between networks is asymmetric for many contexts.

Here, we propose and analyze a model for interconnected consensus systems, which can represent, for example, collective decision-making over a social network that is supported by AI agents, which provide decision support and themselves interact and cooperatively learn. (See Sec. 5 for further description.) Human-AI systems are gaining popularity for decision-making in military [49]–[51] and financial contexts [52]–[54], yet existing theory for interconnected decision systems is insufficient (even, as we shall show, for a simple linear model). For this application, a dystopian-minded engineer would naturally design the social network to wield greater influence over the network of AI agents, *but how can this be achieved? And how might such a system be optimized?* Similar questions arise for any collective dynamics over asymmetrically coupled networks, as well as the following question: *When networks are optimally coupled, is their coupling configuration cooperative or non-cooperative?* That is, do optimally coupled networks mutually influence each other, or does one network direct others without feedback.

In this work, we approach these questions by consider-

- Z. Song is with the Department of Mathematics, Dartmouth College, Hanover, NH, 03755, USA and the Department of Mathematics, University at Buffalo, State University of New York, Buffalo, NY, 14260, USA.
E-mail: zhao.song@dartmouth.edu
- D. Taylor is with the School of Computing and the Department of Mathematics and Statistics, University of Wyoming, Laramie, WY, 82071, USA and the Department of Mathematics, University at Buffalo, State University of New York, Buffalo, NY, 14260, USA.
E-mail: dane.taylor@uwyo.edu

This work was supported in part by the Simons Foundation (award #578333) and the U.S. National Science Foundation (DMS-2052720).

ing networks that are optimally coupled to maximize the convergence rate toward a collective state. We propose a generalized supraLaplacian matrix [32], [38], [39], [55], [56] $\mathbb{L}(\omega, \delta)$, where $\omega \geq 0$ is a *coupling strength* that controls how strongly network layers influence each other and $\delta \in [-1, 1]$ is an *asymmetry parameter* that tunes the extent to which interlayer edges are biased in a particular direction. Motivated by human-AI decision systems, we use $\mathbb{L}(\omega, \delta)$ to formulate a continuous-time linear model for interconnected consensus systems. We find that coupling asymmetry can significantly bias the limiting consensus state and possibly speed or slow the rate $\text{Re}(\lambda_2)$ of convergence (which depends on the real part of λ_2 , since $\mathbb{L}(\omega, \delta)$ can be an asymmetric matrix).

To gain analytical insight, we develop spectral approximation theory for the large ω (i.e., strong coupling) limit to identify and characterize different effects on $\text{Re}(\lambda_2)$ due to varying δ . This reveals several surprising and unintuitive insights. For example, depending on the network layers' structures, increasing the magnitude (i.e., $|\delta|$) of coupling asymmetry can monotonically slow convergence, monotonically speed convergence, or have a more complicated effect on $\text{Re}(\lambda_2)$. For some systems, the direction (i.e., $\text{sign}(\delta)$) of asymmetry is extremely important, whereas it doesn't matter for others. We provide an initial identification and taxonomy for such nonlinear behaviors.

Because technological and natural systems are often highly optimized due to engineering and the process of natural selection, we present theory and experiments to study network layers that are coupled with an optimal level of asymmetry, $\hat{\delta} = \text{argmax}_{\delta} \text{Re}(\lambda_2)$, that maximally accelerates convergence toward a collective state. Focusing on the case of two layers, we characterize these configurations as being either *cooperative*, in which case $|\hat{\delta}| < 1$ so that $\hat{\delta}$ lies within the open set $(-1, 1)$ and the layers mutually influence each other; or *non-cooperative*, in which case $|\hat{\delta}| = 1$ so that $\hat{\delta} \in \{-1, 1\}$ lies on the boundary. In the latter case, the optimal asymmetry involves one network fully directing the other without feedback. Notably, the existence of a cooperative optimum guarantees that the convergence rate of the multiplexed systems is faster than that for either system.

We find that the nonlinear effects of δ on $\text{Re}(\lambda_2)$ and optima $\hat{\delta}$ depend sensitively on the layers' distinct topological structures as well as their separate time scales for consensus. Therefore, we introduce and study a *rate-scaling* parameter χ that allows us to tune whether consensus is faster within layer 1 ($\chi \approx 1$) or layer 2 ($\chi \approx 0$). By considering the range $\delta \in [-1, 1]$ for fixed $\chi \in (0, 1)$, we obtain a criterion (see Sec. 4.2) that can guarantee the existence of a cooperative optimum, which requires that the layers' dynamics have sufficiently similar time scales (i.e., χ is neither too large or small). Finally, we also consider situations where both δ and χ can be freely varied and jointly optimized. We also identify scenarios of cooperative and non-cooperative optima for this more complicated setting, showing that it can be beneficial to design one layer to be as fast as possible and then have that layer non-cooperatively influence other layers without feedback. However, for other network structures, convergence can be fastest by striking a cooperative

balance, both in terms of the asymmetric coupling of layers as well as a balance for their respective time scales. Our work highlights *optimization through coupling asymmetry and time-scale balancing* as important directions for understanding and engineering collective dynamics over human-AI consensus systems and other interconnected networks in general. Moreover, because graph Laplacian matrices are so widely used to study physical, biological and technological systems, our findings are relevant and broadly informative for many other types of dynamics.

This paper is organized as follows. In Sec. 2, we introduce the model that we study. In Sec. 3, we present experiments highlighting various effects of coupling asymmetry. In Sec. 4, we present theoretical results including an existence guarantee for a cooperative optimum. In Sec. 5, we apply the framework to model collective decisions by human-AI teams. A discussion is provided in Sec. 6.

2 MODEL

We first define a model for multiplex networks with asymmetrically coupled layers (Sec. 2.1) and a model for collective dynamics over such networks (Sec. 2.2). Our formulation has three tunable parameters: ω and δ control the strength and asymmetry of coupling between layers, respectively, whereas χ controls the different timescales of dynamics in separate layers.

2.1 Multiplex Networks with Asymmetric Coupling

We begin by defining supraLaplacian matrices for multiplex networks with asymmetrically coupled layers and by formulating an interconnected consensus model for collective dynamics. Consider a multiplex network with T network layers, each consisting of N nodes. For each layer $t \in \{1, \dots, T\}$, we let $\mathbf{A}^{(t)} \in \mathbb{R}^{N \times N}$ be its "intralayer" adjacency matrix and $\mathbf{L}^{(t)} = \mathbf{D}^{(t)} - \mathbf{A}^{(t)}$ be its intralayer unnormalized Laplacian matrix, where $\mathbf{D}^{(t)}$ is a diagonal matrix that encodes the nodes' weighted in-degrees, $D_{ii}^{(t)} = \sum_j A_{ij}^{(t)}$ (also called 'strengths'). Note that our notational convention is to let $A_{ij} > 0$ encode the weight for an edge from node j to i . Matrices $\mathbf{A}^{(t)}$ and $\mathbf{L}^{(t)}$ are size $N \times N$ and are asymmetric if network layer t contains directed edges.

We couple the layers using an "interlayer" adjacency matrix $\mathbf{A}^I(\delta) = (1+\delta)\hat{\mathbf{A}}^I + (1-\delta)[\hat{\mathbf{A}}^I]^T$, where $\delta \in [-1, 1]$ is an *asymmetry parameter* that tunes the magnitude and direction of coupling asymmetry and $\hat{\mathbf{A}}^I$ is an adjacency matrix for a graph in which all edges are strictly directed (i.e., there no bidirectional edges or self edges). Each positive matrix element $\hat{A}_{st}^I > 0$ encodes a directed influence from network layer t to layer s . When $\delta \neq 0$, the coupling between layers is biased in a particular direction that is encoded by $\hat{\mathbf{A}}^I$, whereas the coupling is symmetric when $\delta = 0$. We refer the situation of $\delta \in \{-1, 1\}$ as *fully asymmetric coupling*, and it can possibly yield situations in which a network layer influences other layers but itself is not influenced by any other layer. Note also that we can equivalently define $\mathbf{A}^I(\delta) = \mathbf{A}_+^I + \delta \mathbf{A}_-^I$, where $\mathbf{A}_+^I = \hat{\mathbf{A}}^I + [\hat{\mathbf{A}}^I]^T$ and $\mathbf{A}_-^I = \hat{\mathbf{A}}^I - [\hat{\mathbf{A}}^I]^T$ are symmetric and skew-symmetric matrices, respectively.

Given $A^I(\delta)$, we define an associated interlayer unnormalized Laplacian $L^I(\delta) = D^I(\delta) - A^I(\delta)$, where $D^I(\delta)$ is a diagonal matrix with entries $D_{ss}^I(\delta) = \sum_t A_{st}^I(\delta)$. It is also useful to define an equivalent formulation,

$$L^I(\delta) = L_+^I + \delta L_-^I, \quad (1)$$

where $L_+^I = D_+^I - A_+^I$, $L_-^I = D_-^I - A_-^I$, $[D_+^I]_{ss} = \sum_t [A_+^I]_{st}$, and $[D_-^I]_{ss} = \sum_t [A_-^I]_{st}$. Note that L_+^I is a Laplacian matrix that is associated with an undirected graph, whereas L_-^I may be interpreted as a Laplacian for a directed, signed graph that has a very particular structure: for any positive edge weight $[A_-^I]_{st} > 0$, the reciprocal edge must exist and have negative weight $[A_-^I]_{ts} = -[A_-^I]_{st}$. (We note that there are other ways to define signed Laplacians [57], [58].) In the case of $T = 2$ layers, such as the multiplex network shown in Fig. 1, we define $\hat{A}^I = \begin{pmatrix} 0 & 0 \\ 1 & 0 \end{pmatrix}$ and

$$L^I(\delta) = \begin{pmatrix} 1 & -1 \\ -1 & 1 \end{pmatrix} + \delta \begin{pmatrix} -1 & 1 \\ -1 & 1 \end{pmatrix}. \quad (2)$$

We next define a supraLaplacian matrix following [38] by scaling each $L^I(\delta)$ by a coupling strength $\omega > 0$ to construct a supraLaplacian matrix

$$\mathbb{L}(\omega, \delta) = \mathbb{L}^L + \omega \mathbb{L}^I(\delta), \quad (3)$$

where $\mathbb{L}^L = \text{diag}[\mathbf{L}^{(1)}, \dots, \mathbf{L}^{(T)}]$ contains intralayer Laplacians as diagonal blocks, and $\mathbb{L}^I(\delta) = L^I(\delta) \otimes \mathbf{I}$ couples the layers in a way that is *uniform* (i.e., any coupling between two given layers is the same) and *diagonal* (i.e., any coupling between layers connects a node in one layer to itself in another layer) [59], [60]. Symbol \otimes indicates the Kronecker product. Note that $\mathbb{L}(\omega, \delta)$ is a size- (NT) square matrix, and we will enumerate its rows and columns by $p \in \{1, \dots, NT\}$.

Under the choice $\delta = 0$, $\mathbb{L}(\omega, \delta)$ is a symmetric matrix, and it recovers previously studied supraLaplacians [32], [38], [39], [55], [56], which that have been used to study diffusion and random walks over multiplex networks with layers that are symmetrically coupled using undirected interlayer edges. Understanding the spectral properties of supraLaplacians has revealed novel insights including “superdiffusion” [55], [56], [61], whereby diffusion over coupled networks is faster than that of any single network layer, if it were in isolation. The study of synchronization over multiplex networks has similarly led to discoveries including the observation the networks coupled with moderate coupling strength have better synchronizability [39] and other insights [33]–[37]. Despite this progress, the effects of asymmetric coupling on multiplex-network dynamics remains under-explored.

2.2 Asymmetrically Coupled Consensus Systems

Consensus is a popular model for collective decision making in the cognitive, social and biological sciences [4], [6]–[8], and it also provides a foundation for decentralized algorithms for neural networks and machine learning [10]–[15]. Thus motivated, we propose a model for interconnected consensus systems via the following linear ordinary differential equation,

$$\frac{d}{d\tau} \mathbf{x}(\tau) = -\mathbb{L}(\omega, \delta) \mathbf{x}(\tau), \quad (4)$$

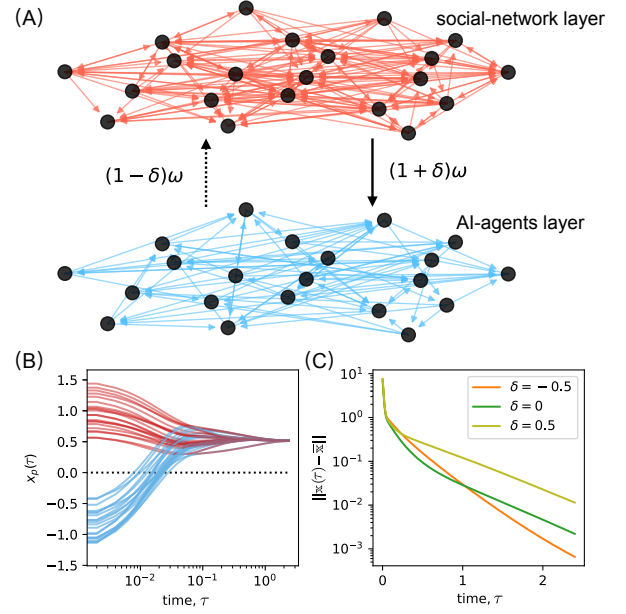


Fig. 1. **Asymmetric coupling biases the limit and convergence rate for interconnected consensus systems.** (A) A two-layer network in which layer 1 is an empirical social network that encodes mentoring relationships among corporate executives [62]. Layer 2 models a communication network over which AI-agents cooperatively learn, which we generate as a random directed graph. The AI-agents provide decision support to the executives through “interlayer” edges of weight $(1 \pm \delta)\omega$, where ω and δ encode the strength and asymmetry, respectively, of coupling between the two networks. (B) Nodes’ states $x_p(\tau)$ reach consensus (i.e., a collective decision) following (4), which uses a supraLaplacian matrix $\mathbb{L}(\omega, \delta)$ with $(\omega, \delta) = (30, 0.5)$ and converges to a limit \bar{x} that is a weighted average of the initial condition with weights that are biased by δ . (C) Convergence $x_p(\tau) \rightarrow \bar{x}$ is shown to occur faster for $\delta = -0.5$ than for $\delta \in \{0, 0.5\}$. For each δ , the convergence rate $\text{Re}(\lambda_2)$ gives the curve’s asymptotic slope for large τ .

where $\mathbf{x}(\tau) = [x_1(\tau), \dots, x_p(\tau), \dots, x_{NT}(\tau)]^T$ is a length- NT vector. Each $x_p(\tau)$ encodes the state of node $i_p = (p \bmod N)$ in layer $t_p = \lceil p/N \rceil$ at time τ . (We let $p \in \{1, \dots, NT\}$ and use $\text{mod}(\cdot)$ and $\lceil \cdot \rceil$ to denote the modulus and ceiling function, respectively.) In Sec. 5, we interpret (4) as a simple-yet-informative model for collective decisions in a human-AI system in which individuals in a social network are supported by AI agents, who themselves coordinate and collectively learn.

Equation (4) can be considered as the “multiplexing” of two consensus processes: consensus within each network layer and consensus across layers. That is, one could define an intralayer consensus dynamics for each network layer t : $\frac{d}{d\tau} \mathbf{x}^{(t)}(\tau) = -\mathbf{L}^{(t)} \mathbf{x}^{(t)}(\tau)$ with initial condition $\mathbf{x}^{(t)}(0) \in \mathbb{R}^N$. Similarly, one can define an interlayer consensus dynamics by $\frac{d}{d\tau} \mathbf{x}(\tau) = -\omega \mathbf{L}^I(\delta) \mathbf{x}(\tau)$ with some initial condition $\mathbf{x}(0) \in \mathbb{R}^T$. In this context, the scaling by ω controls the timescale of consensus across layers as compared to consensus within layers. As such, it is important to consider dynamics for a wide range of ω values. We also note that each of these differential equations can be interpreted as a type of Abelson model [63], [64] for opinion dynamics.

One can also vary the timescales for dynamics and consensus within each separate layer by scaling each $\mathbf{L}^{(t)}$ by some nonnegative constant. Focusing on the case of $T = 2$ layers, replace the intralayer Laplacians by $\mathbf{L}^{(1)} \mapsto \chi \mathbf{L}^{(1)}$

and $\mathbf{L}^{(2)} \mapsto (1 - \chi)\mathbf{L}^{(2)}$ where $\chi \in (0, 1)$ is a *rate-scaling parameter* that controls whether the layers' timescales are equally balanced ($\chi \approx 0.5$), whether layer 1 is much faster than layer 2 ($\chi \approx 1$), or vice versa ($\chi \approx 0$). We will initially not include χ in our model and will investigate it later in Sec. 4.2 and Sec. 5.

Although we focus here on consensus dynamics, it would be straightforward to utilize matrix $\mathbb{L}(\omega, \delta)$ to formulate models for diffusion, synchronization and other Laplacian-based dynamical processes over multiplex networks with asymmetrically coupled layers. For example, the substitution of $\mathbb{L}(\omega, \delta) \mapsto \mathbb{L}(\omega, \delta)^T$ in (4) would yield a model for diffusion.

3 EFFECTS OF COUPLING ASYMMETRY

We first show how coupling asymmetry can have various effects on solutions to (4). In Sec. 3.1, we highlight that asymmetry can bias the consensus limit and either increase or decrease the convergence rate. In Sec. 3.2, we discuss the optimization of coupling asymmetry δ to maximize the convergence rate. In Sec. 3.3, we study the effects on random multiplex networks.

3.1 Impact on Consensus Limit and Convergence Rate

We assume that the smallest eigenvalue $\lambda_1 = 0$ of $\mathbb{L}(\omega, \delta)$ is simple (i.e., has algebraic and geometric multiplicities equal to one), which is guaranteed, e.g., if the interlayer network and aggregated network are both strongly connected [32]. Then for any real-valued initial condition $\mathbf{x}(0)$, (4) converges to an equilibrium $\mathbf{x}(\tau) \rightarrow \bar{\mathbf{x}} = [\bar{x}, \dots, \bar{x}]^T$, which is the right eigenvector associated with λ_1 . The *consensus limit* is reached at a scalar value

$$\bar{x} = \sum_p u_p x_p(0) / \sum_{p'} u_{p'}, \quad (5)$$

which is a weighted average of the initial states, and the weights u_p are entries of the left eigenvector \mathbf{u} of $\mathbb{L}(\omega, \delta)$ that is associated with λ_1 . The *asymptotic convergence rate*,

$$-\limsup_{\mathbf{x}(0)} \frac{1}{\tau^*} \int_0^{\tau^*} \log \left(\frac{\|\mathbf{x}(\tau) - \bar{\mathbf{x}}\|}{\|\mathbf{x}(0) - \bar{\mathbf{x}}\|} \right) d\tau \leq \text{Re}(\lambda_2), \quad (6)$$

is bounded by $\text{Re}(\lambda_2)$, the real part of the eigenvalue of $\mathbb{L}(\omega, \delta)$ that has second-smallest real part. Throughout this manuscript, we refer to $\text{Re}(\lambda_2)$ simply as the “convergence rate”, keeping in mind that it is a bound on the asymptotic behavior of convergence.

In Fig. 1, we show how coupling asymmetry can bias the collective state \bar{x} as well as the convergence rate $\text{Re}(\lambda_2)$. In this example, we study (4) for $T = 2$ network layers with $\mathbf{L}^I(\delta)$ given by (2). The first intralayer consensus system models group decision making within an empirical social network that encodes mentoring relationships among corporate executives [62]. It contains $N = 21$ nodes and 190 directed edges and was downloaded from [65]. The second intralayer consensus system represents AI agents that support the executives' decisions, and we model their communication by a directed 4-regular graph that we generated using the configuration model. We note that we have

selected this empirical example because collective human-AI decision making is already widespread in military [49]–[51] and financial contexts [52]–[54], and we predict that it will become increasingly popular in corporate settings in the near future.

In Fig. 1(B), we show converging trajectories $x_p(\tau)$ under the parameter choices $(\omega, \delta) = (30, 0.5)$ for an initial condition where $x_p(\tau)$ are positive for nodes in layer 1 and negative for nodes in layer 2. Observe that the limit $\bar{x} > 0$ is biased to be positive, implying that the social network has a “stronger say” than the AI agents regarding the state at which consensus is reached. This occurs here because we chose $\delta > 0$, implying that the social network more strongly influences the AI agents, that is, as compared to the reciprocal relationship. However, observe in Fig. 1(C) that convergence is slower for this value of δ as compared to the other shown values: $\delta \in \{0, -0.5\}$. Later in Sec. 5, we will present an extended study of the network shown in Fig. 1, showing that $\text{Re}(\lambda_2)$ has a maximum near $\delta \approx -0.6$. We will also further discuss the implications of our work for the application area of human-AI systems.

3.2 Optimizing Asymmetry for Fast Convergence

For many applications it is beneficial for consensus to converge quickly, and we are particularly interested in understanding the value (or values) of δ that maximize the convergence rate: $\hat{\delta} = \text{argmax}_\delta \text{Re}(\lambda_2)$. To this end, it is beneficial to first gain a broader understanding for the diverse ways that δ can influence $\text{Re}(\lambda_2)$. Below, we offer a characterization of several possible ways for how the convergence rate $\text{Re}(\lambda_2)$ toward a collective state can be affected by the asymmetric coupling of network layers. The columns of Fig. 2 highlight five distinct behaviors for how asymmetric coupling can affect $\text{Re}(\lambda_2)$ and its optima $\hat{\delta} = \text{argmax}_\delta \text{Re}(\lambda_2)$. These are:

- (i) *layer dominance*: $\text{Re}(\lambda_2)$ monotonically increases or decreases with δ and obtains a maximum at either $\hat{\delta} = \pm 1$;
- (ii) *robust cooperative optimum*: $\text{Re}(\lambda_2)$ obtains a maximum at some value $\hat{\delta} \in (-1, 1)$, and $\text{Re}(\lambda_2)$ is differentiable with respect to δ at the optimum;
- (iii) *nonrobust cooperative optima*: $\text{Re}(\lambda_2)$ obtains a maximum at some value $\hat{\delta} \in (-1, 1)$, but $\text{Re}(\lambda_2)$ is not differentiable with respect to δ at the optimum;
- (iv) *strictly positive effect*: $\text{Re}(\lambda_2)$ is a non-decreasing function of $|\delta|$ (i.e., slowest convergence at $\delta = 0$);
- (v) *strictly negative effect*: $\text{Re}(\lambda_2)$ is a non-increasing function of $|\delta|$ (i.e., fastest convergence at $\delta = 0$).

Notably, these characterizations are an incomplete list. Future work will likely reveal other possible behaviors, thereby broadening our understanding of how the asymmetric coupling of networks can impact a combined system's convergence rate and other dynamical properties for collective dynamics.

We provide examples that exhibit the behaviors (i)–(v) in the five columns, respectively, of Fig. 2. We visualize the multiplex networks in Fig. 2(A), and for each system, we plot $\text{Re}(\lambda_2)$ versus δ in Fig. 2(B) for different choices of ω . The solid black curves in Fig. 2(B) are a theoretical predict

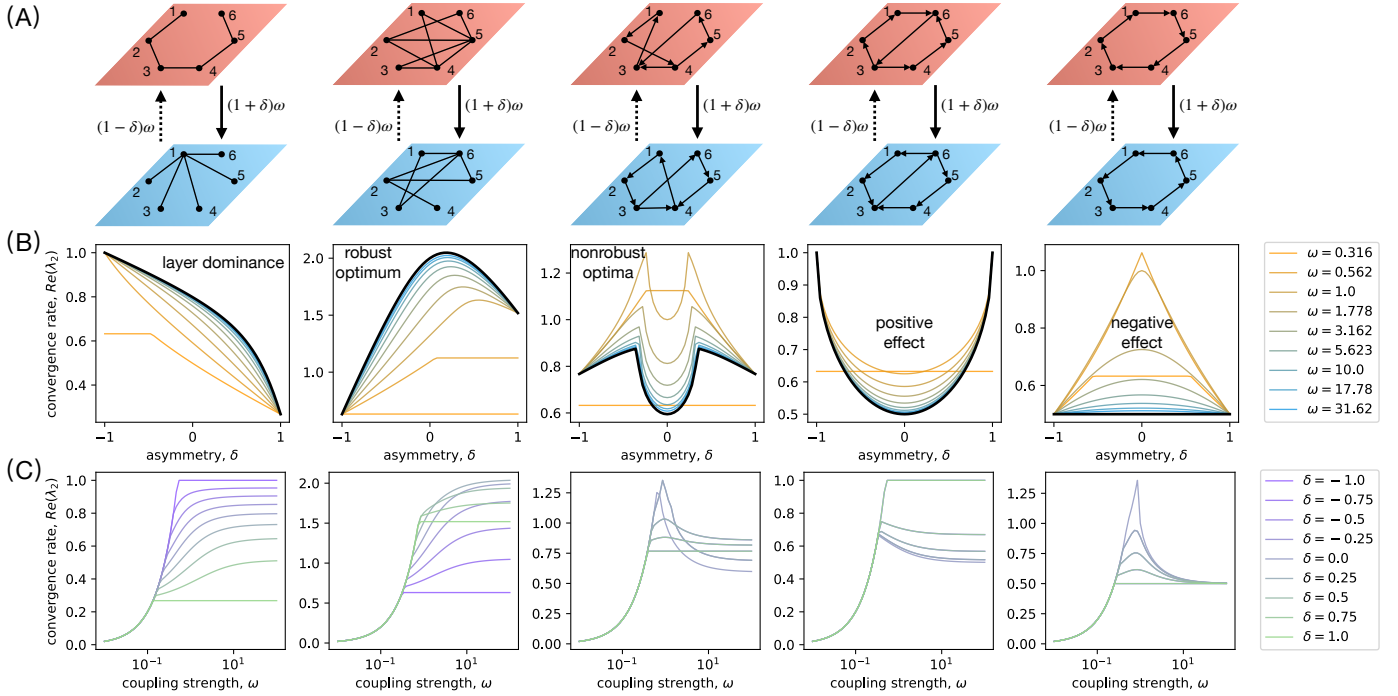


Fig. 2. Characteristic ways in which coupling asymmetry can affect convergence rate. (A) Interconnected consensus systems with $N = 6$ nodes and $T = 2$ layers that are asymmetrically coupled through the interlayer Laplacian matrix defined in (2). (B) For each respective system, we plot the convergence rate $\text{Re}(\lambda_2)$ versus δ . Colored curves depict different ω (see legend). Observe for different networks that asymmetry (i.e., $\delta \neq 0$) has remarkably diverse effects in which it either speeds/slow convergence depending on the sign and magnitude of δ (e.g., see columns 1 and 2), always accelerates convergence (e.g., see columns 3 and 4), or always slows convergence (e.g., see column 5). Black curves depict our theoretical prediction for large ω given by (7)–(9). (C) For each system, we plot $\text{Re}(\lambda_2)$ versus coupling strength ω . Observe for all systems that δ impacts $\text{Re}(\lambda_2)$ only when ω is sufficiently large and that some systems exhibit an *intermediate coupling optimum* (ICO), which is a peak that can either be exaggerated or diminished by introducing coupling asymmetry.

that we will present in Sec. 4.1. The systems depicted in columns 1 and 4 of Fig. 2 exhibit behaviors (i) and (iv), respectively, which exhibit non-cooperative optima. That is, convergence toward the collective state occurs optimally fast only when one layer influences the other without a reciprocated influence (i.e., $\hat{\delta} \pm 1$). In contrast, the systems depicted in columns 2, 3 and 5 exhibit behaviors (ii), (iii) and (v), which have cooperative optima. Convergence is fastest when the layers mutually influence one another (i.e., $|\hat{\delta}| < 1$). We further note that it is beneficial to distinguish between robust vs non-robust optima, and we call an optimum “robust” if and only if $\frac{d}{d\delta}\text{Re}(\lambda_2)$ is zero at the optimum. Robustness is important when considering the possible effects on $\text{Re}(\lambda_2)$ of uncertainty for δ near the optimum.

In Fig. 2(C), we plot $\text{Re}(\lambda_2)$ versus ω to investigate the relation between coupling asymmetry δ and coupling strength ω . First, observe that there exists a peak for the third, fourth and fifth systems for some intermediate value of ω , but not the first or second system. Such a peak corresponds to an optimal choice of ω at which the convergence rate maximized. We refer to this phenomenon as an *intermediate coupling optimum* (ICO), and this spectral property for λ_2 has been previously called “superdiffusion” [55], [56], [61] in the context of diffusion on multiplex networks. In fact, the first, second and fifth systems were previously used to study diffusion over multiplex networks in [32], [38] and [55], respectively. Those studies were restricted to the assumption of symmetric coupling in which $\delta = 0$. Extending that work,

here we show that there exists a similar ICO phenomenon for multiplexed consensus systems, and that the size of the peak can be either exaggerated or inhibited depending on the direction and magnitude of coupling asymmetry.

3.3 Effects on Random Multiplex Networks

We conclude this section by studying $\text{Re}(\lambda_2)$ for random multiplex networks with $T = 2$ layers, each of which is generated by two of the following generative models:

- (i) Erdős-Rényi (ER) graphs [66] in which each edge is independently created as a Bernoulli random variable probability p .
- (ii) Barabási-Albert (BA) graphs [67], which are grown by attaching each new node to m edges that are preferentially selected based on their degree.
- (iii) Watts-Strogatz small-world (SW) graphs [68], which are created by first assigning nodes positions along a ring and by creating edges between each node and its k nearest neighbors. Then, each edge is replaced by a new, randomly selected edge with probability p .

We selected these three models, since they give rise to different well-known properties: degree-homogeneity for ER graphs; degree-heterogeneity for BA graphs; and the small-world property for SW graphs. Unless otherwise specified, we construct multiplex networks with $N = 500$ nodes and choose $p = 0.02$ for the ER layers, $m = 4$ edges for the BA layers, and $(p, k) = (0.2, 8)$ for the SW layers. Additional parameter choices are studied in Appendix D.

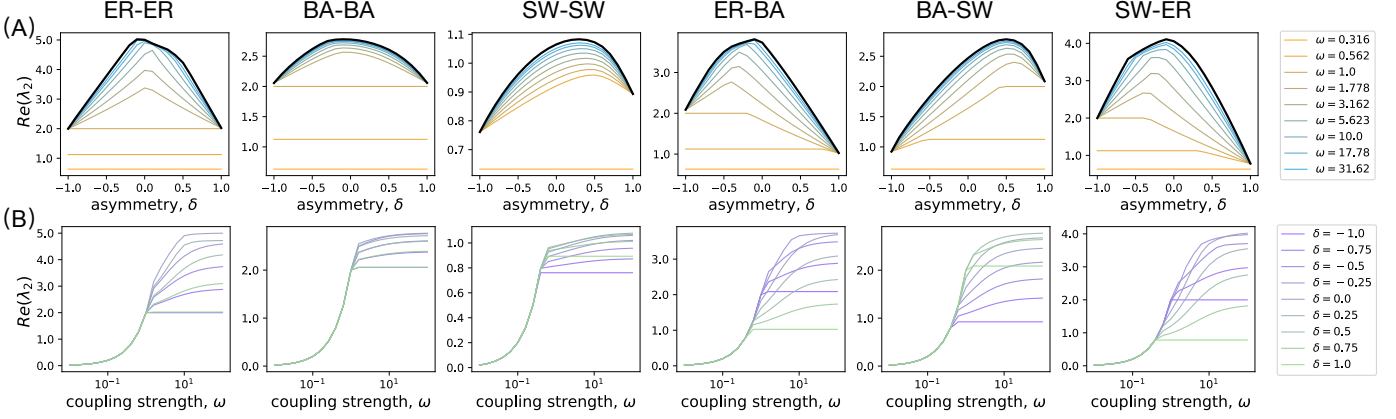


Fig. 3. Cooperative optima for random multiplex networks with layers sampled from random-graph models. We study $\text{Re}(\lambda_2)$ versus either (A) δ or (B) ω for six multiplex networks, each having $T = 2$ layers coupled by the interlayer Laplacian matrix defined in (2). Each network layer is sampled from one of three generative models: Erdős-Rényi graphs (ER), Barabási-Albert graphs (BA), and Watts-Strogatz small-world graphs (SW). Black curves in (A) depict a theoretical prediction for large ω that we will develop in Sec. 4.

In Fig. 3, we study $\text{Re}(\lambda_2)$ for six multiplex networks in which each layer is generated by one of the three generative models. (For example, “ER-BA” indicates that the first layer is an ER graph, whereas the second is a BA graph.) Similar to Figs. 2(B) and (C), we plot $\text{Re}(\lambda_2)$ versus δ in Fig. 3(A) and $\text{Re}(\lambda_2)$ versus ω in Fig. 3(B). Our main observation in Fig. 3(A) is that these six random multiplex networks all exhibit a cooperative optimum for sufficiently large ω .

In Sec. 4, we will develop and apply theory to shed light on the various dynamical and structural mechanisms that can give rise to behaviors (i)–(v) and yield optimally coupled systems that are either cooperative or non-cooperative. Our analytical approach is motivated by the following observations. Observe in each panel of Figs. 2(B) and 3(A) that the different curves reflect different choices for the interlayer coupling strength ω and that the qualitative effects on $\text{Re}(\lambda_2)$ of δ are consistent across a wide range of ω values. Moreover, observe in each panel of Figs. 2(C) and 3(B) that there exists a critical value of ω below which δ has no observable effect on $\text{Re}(\lambda_2)$. That is, the various effects of coupling asymmetry only arise when ω is sufficiently large. [Interestingly, the fifth system in Fig. 2 is an exception, since δ appears to affect $\text{Re}(\lambda_2)$ only for intermediate values of ω near the ICO peak.] With this in mind, in the next section we present theory to predict the effects of coupling asymmetry on $\text{Re}(\lambda_2)$ for when the layers are strongly coupled with large ω .

4 THEORETICAL RESULTS

We now present our main theoretical findings. In Sec. 4.1, we analyze $\text{Re}(\lambda_2)$ in the limit of strong interlayer coupling. In Sec. 4.2, we build on these results to provide criterion that guarantees the existence of a cooperative optimum. Our derivations are deferred to appendices.

4.1 Theory for Strong Coupling, $\omega \rightarrow \infty$.

To provide analytical guidance, we characterize the dependence of $\text{Re}(\lambda_2)$ on δ using spectral perturbation theory for multilayer networks with asymmetric matrices [32], [60]. We present the derivations in Appendix B and summarize our

findings here. The black curves in Fig. 2(B) and Fig. 3(A) depict our predictions for large ω ,

$$\lim_{\omega \rightarrow \infty} \lambda_2 = \bar{\lambda}_2(\delta), \quad (7)$$

where $\bar{\lambda}_2(\delta)$ is the eigenvalue of $\bar{\mathbf{L}}(\delta)$ that has the second-smallest real part, and

$$\bar{\mathbf{L}}(\delta) = \sum_{t=1}^T w_t(\delta) \mathbf{L}^t \quad (8)$$

is a weighted average of the layers’ Laplacian matrices. The weights $w_t(\delta) = u_t(\delta) / \sum_{t'} u_{t'}(\delta)$ come from the entries of the left eigenvector $\mathbf{u}(\delta) = [u_1(\delta), \dots, u_T(\delta)]^T$ that is associated with the zero-valued (i.e., trivial) eigenvalue of $\mathbf{L}^I(\delta)$. (See [38], [39] for results that are similar to (8) but which assume symmetric coupling, $\delta = 0$).

Equations (7)–(8) imply that when a multiplex consensus system is strongly coupled, the convergence rate is identical to that for consensus on an “effective” network that is associated with a Laplacian matrix $\bar{\mathbf{L}}(\delta)$, and the effects of δ can be examined by considering the dependence of $w_t(\delta)$ on δ . For example, for $T = 2$ layers, the interlayer Laplacian $\mathbf{L}^I(\delta)$ is given by (2), $\mathbf{u}(\delta) = [1 + \delta, 1 - \delta]^T$ and we find

$$\bar{\mathbf{L}}(\delta) = \left(\frac{1 + \delta}{2} \right) \mathbf{L}^{(1)} + \left(\frac{1 - \delta}{2} \right) \mathbf{L}^{(2)}. \quad (9)$$

Despite this simple form, the associated convergence rate $\text{Re}(\bar{\lambda}_2(\delta))$ can exhibit a complicated dependence on δ . For example, observe in Fig. 2(B) and Fig. 3(A) that in addition to being accurate for large ω , this theory predicts the qualitative behavior of the relationship between $\text{Re}(\lambda_2)$ and δ for a broad range of ω . At the same time, also observe that the characterization of the optimum as being cooperative vs. non-cooperative in the limit $\omega \rightarrow \infty$ also is predictive of that optimum for other choices of ω .

One consequence of (7)–(9) is the following limiting behavior for when either layer 1 or layer 2 directs the other layer without feedback:

$$\lim_{\delta \rightarrow 1} \bar{\lambda}_2(\delta) \rightarrow \lambda_2^{(1)}, \quad (10a)$$

$$\lim_{\delta \rightarrow -1} \bar{\lambda}_2(\delta) \rightarrow \lambda_2^{(2)}, \quad (10b)$$

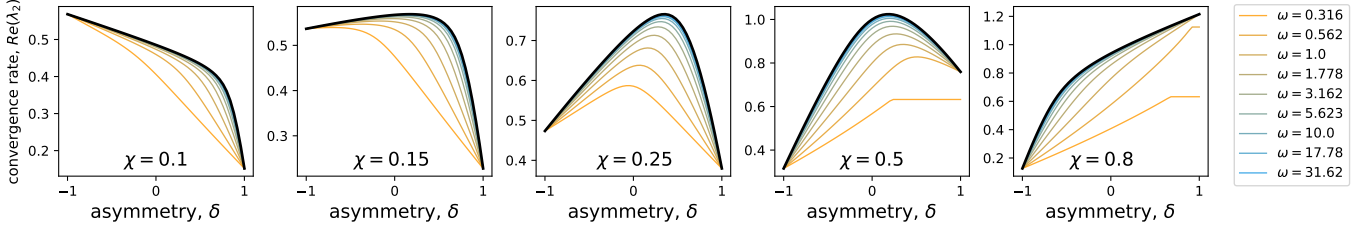


Fig. 4. Layers' relative timescales influence if optima are cooperative vs. non-cooperative. We plot the convergence rate $\text{Re}(\lambda_2)$ versus δ for the system that was visualized in the second column of Fig. 2(A). Different columns correspond to different choices for a rate-scaling parameter $\chi \in (0, 1)$, which we introduce to tune whether layer 1 is much faster ($\chi \approx 1$) or layer 2 is much faster ($\chi \approx 0$). Colored curves yield results for different ω (see legend), and black curves depict our theoretical prediction for large ω that is given by (7)–(9). By comparing across the columns, observe that their optima are cooperative for intermediate values of χ (i.e., the second, third and fourth columns) and non-cooperative when χ is sufficiently small or large (see left-most and right-most columns).

where $\lambda_2^{(1)}$ and $\lambda_2^{(2)}$ are the second-smallest eigenvalues of $\mathbf{L}^{(1)}$ and $\mathbf{L}^{(2)}$, respectively. This follows immediately after considering that $\lim_{\delta \rightarrow -1} \bar{\mathbf{L}}(\delta) = \mathbf{L}^{(1)}$ and $\lim_{\delta \rightarrow -1} \bar{\mathbf{L}}(\delta) = \mathbf{L}^{(2)}$. Thus, the convergence rate of a single layer dictates the overall system's convergence when the coupling asymmetry implements non-cooperation.

Given the above theory, we can now better understand the results that were previously shown in Fig. 2(B). Recall that the black curves in that figure represent our analytical prediction $\text{Re}(\bar{\lambda}_2(\delta))$. Moreover, for all five systems, we predict that $\text{Re}(\lambda_2)$ converges to $\text{Re}(\lambda_2^{(2)})$ and $\text{Re}(\lambda_2^{(1)})$ in the limits $\delta \rightarrow -1$ and $\delta \rightarrow 1$, respectively. Interesting, our derivation of (10) has assumed the limit of large ω , but one can observe in Fig. 2(B) that it accurately predicts the limiting $\delta \rightarrow \pm 1$ behavior of $\text{Re}(\lambda_2)$ for a wide range of coupling strengths ω . That is, most of the curves that represent different ω values converge to the same point on the left-hand and right-hand sides of each subpanel. We only observe (10) to yield an inaccurate prediction for the $\delta \rightarrow \pm 1$ limits of λ_2 when ω is very small [e.g., when $\omega = 0.316$ in columns 1, 3 and 4 of Fig. 2(B) or $\omega = \{0.316, 0.562\}$ in column 2 of Fig. 2(B)]. Similar results can also be observed in Fig. 3(A). For all six multiplex networks, $\text{Re}(\lambda_2)$ converges to $\text{Re}(\lambda_2^{(2)})$ and $\text{Re}(\lambda_2^{(1)})$ in the limits $\delta \rightarrow -1$ and $\delta \rightarrow 1$, respectively, for a wide range of coupling strengths ω .

Equation (10) also hints at why an optimally coupled system will exhibit layer dominance rather than a cooperative optimum. Consider the first column of Fig. 2, where we observed a non-cooperative optimum: $\text{Re}(\lambda_2)$ obtains its maximum at $\delta = -1$, whereby layer 2 influences layer 1 without feedback. In this case, layer 1 is an undirected chain graph that has a convergence rate of $\lambda_2^{(1)} \approx 0.26$, whereas layer 2 is a star graph that has a convergence rate of $\lambda_2^{(2)} \approx 1$. Thus, the convergence rate is faster for the star graph than the chain graph, and this particular system converges fastest when the faster system (layer 2) non-cooperatively influences the slower one without feedback. In the next section, we develop theory that can help determine whether the optimum is cooperative and how that relates to the layers' individual timescales.

4.2 Existence Guarantee for a Cooperative Optimum

We first show that a cooperative optimum vs. layer dominance occurs when the layers have a sufficiently similar

timescale, and in fact, we can adjust a system between these two behaviors by varying their timescales. Recall from the model definition in Sec. 2.2 that we can use a *rate-scaling parameter* $\chi \in (0, 1)$ to vary the relative convergence rate for each layer. That is, we define the the intralayer Laplacians $\chi \mathbf{L}^{(1)}$ and $(1 - \chi) \mathbf{L}^{(2)}$ so that their separate convergence rates are $\chi \text{Re}(\lambda_2^{(1)})$ and $(1 - \chi) \text{Re}(\lambda_2^{(2)})$, respectively. It also then follows that (9) takes the form $\bar{\mathbf{L}}(\delta) = \frac{1+\delta}{2} \chi \mathbf{L}^{(1)} + \frac{1-\delta}{2} (1 - \chi) \mathbf{L}^{(2)}$.

In Fig. 4, we plot the convergence rate $\text{Re}(\lambda_2)$ versus δ for the system that was visualized in the second system in Fig. 2(A). Different columns correspond to different choices for χ . In each panel, different curves reflect different choices for ω . Black curves indicate the analytical prediction for large ω given by (8). By comparing across the columns of Fig. 4, observe that their optima are cooperative for intermediate values of χ (i.e., the second, third and fourth columns) and non-cooperative when χ is sufficiently small or large (see the left-most and right-most columns). That is, we observe a cooperative optimum for these systems when the convergence rates for the two separate layers are sufficiently similar. Otherwise, in this experiment, we find that the convergence is fastest when the faster layer influences the slower one without a reciprocated influence, i.e., layer dominance. This observation is further supported in Appendix D, where we provide additional figures similar to Fig. 4 for the family of random multiplex networks described in Sec. 3.3.

We now present a criterion that predicts how the optimal asymmetric coupling of layers can change between cooperative and non-cooperative as one varies χ . We present this theory in Appendix C and summarize our main findings here. We predict the existence/nonexistence of an optimum in the limit of large ω by considering the derivative

$$\bar{\lambda}'_2(\delta) \equiv \frac{d}{d\delta} \text{Re}(\bar{\lambda}_2(\delta)) \quad (11)$$

and by invoking Rolle's Theorem [69] for a continuous function: if $\bar{\lambda}'_2(-1) > 0$ and $\bar{\lambda}'_2(1) < 0$, then there exists at least one optimum $\hat{\delta} = \text{argmax}_\delta \text{Re}(\lambda_2)$ that is cooperative, i.e., $\hat{\delta} \in (-1, 1)$. In the limits $\delta \rightarrow \pm 1$, the derivatives $\bar{\lambda}'_2(\delta)$ converge to a simplified form:

$$\bar{\lambda}'_2(1) = \frac{-\mathbf{u}^{(1)*} \mathbf{L}^{(2)} \mathbf{v}^{(1)}}{2\mathbf{u}^{(1)*} \mathbf{v}^{(1)}} + \chi \frac{\mathbf{u}^{(1)*} (\mathbf{L}^{(1)} + \mathbf{L}^{(2)}) \mathbf{v}^{(1)}}{2\mathbf{u}^{(1)*} \mathbf{v}^{(1)}}, \quad (12a)$$

$$\bar{\lambda}'_2(-1) = \frac{-\lambda_2^{(2)}}{2} + \chi \frac{\mathbf{u}^{(2)*} (\mathbf{L}^{(1)} + \mathbf{L}^{(2)}) \mathbf{v}^{(2)}}{2\mathbf{u}^{(2)*} \mathbf{v}^{(2)}}. \quad (12b)$$

Letting $t \in \{1, 2\}$, here we define $\mathbf{u}^{(t)}$ and $\mathbf{v}^{(t)}$ as the left and right eigenvectors, respectively, that are associated with the eigenvalue $\lambda_2^{(t)}$ of $\mathbf{L}^{(t)}$ that has the second-smallest real part (assumed to be nonzero). Symbol $*$ denotes a vector's complex conjugate. Interestingly, (12) imply that the derivatives $\bar{\lambda}'_2(\delta)$ at $\delta = \pm 1$ change linearly with the time-scaling parameter χ .

By combining (12) with Rolle's Theorem, we can identify for each χ , whether a cooperative optimum is guaranteed to exist. Moreover, we can use the linear form of (12) to predict the values of χ at which $\bar{\lambda}'_2(1)$ and $\bar{\lambda}'_2(-1)$ change sign, allowing us to obtain a simplified criterion for this trait. That is, we solve for $\text{Re}(\bar{\lambda}'_2(\pm 1)) = 0$ to obtain x-intercepts for χ

$$\hat{\chi}(1) = \text{Re} \left(\frac{\mathbf{u}^{(1)*} \mathbf{L}^{(2)} \mathbf{v}^{(1)}}{\mathbf{u}^{(1)*} (\mathbf{L}^{(1)} + \mathbf{L}^{(2)}) \mathbf{v}^{(1)}} \right), \quad (13a)$$

$$\hat{\chi}(-1) = \text{Re} \left(\frac{\mathbf{u}^{(2)*} \mathbf{L}^{(2)} \mathbf{v}^{(2)}}{\mathbf{u}^{(2)*} (\mathbf{L}^{(1)} + \mathbf{L}^{(2)}) \mathbf{v}^{(2)}} \right). \quad (13b)$$

Considering the lines defined in (12), when the slopes are positive and y-intercepts are negative (which we observe to be true for all our experiments, but in principle, it may not always be true), then the implications of Rolle's Theorem can be summarized in a simplified form: a cooperative optimum is guaranteed to exist when the the two layers have sufficiently similar timescales in that

$$\chi \in (\hat{\chi}(-1), \hat{\chi}(1)). \quad (14)$$

That is, χ is neither too large nor too small. Moreover, the criterion given by (14) also guarantees that the convergence rate $\text{Re}(\bar{\lambda}_2(\delta))$ of the multiplexed system is faster than that for either system,

$$\text{Re}(\bar{\lambda}_2(\delta)) > \max\{\chi \text{Re}(\lambda_2^{(1)}), (1 - \chi) \text{Re}(\lambda_2^{(1)})\}. \quad (15)$$

In Fig. 5, we study the combined effects of the asymmetry parameter δ and rate-scaling parameter χ on the convergence rate for the multiplex network that was visualized in the second column of Fig. 2(A). In Fig. 5(A), we plot $\text{Re}(\bar{\lambda}_2(\delta))$ versus δ for several choices of χ . Observe for $\chi \in \{0.15, 0.25, 0.5\}$ that the optimum is cooperative, which agrees with our predicted range given by (14). This range is indicated by the shaded region in Fig. 5(B), where solid and dashed black lines illustrate (12), and their intersections with the x-axis yield the critical values of χ that are defined by (13). The colored lines depict empirically observed values of $\frac{d}{d\delta} \text{Re}(\lambda_2)$ that were computed directly from $\mathbb{L}(\omega, \delta)$ with several choices of coupling strength ω . Interestingly, our theoretical predictions for $\hat{\chi}(\pm 1)$ appear to describe the x-axis intercepts for all of these ω values, which is surprising since our derivation has assumed the limit large ω .

In Fig. 5(C), we visualize by color the convergence rate $\text{Re}(\bar{\lambda}_2(\delta))$ across the parameter space $\delta \in [-1, 1]$ and $\chi \in [0, 1]$. The dashed white curve indicates the optimal asymmetry $\hat{\delta} = \text{argmax}_\delta \text{Re}(\bar{\lambda}_2(\delta))$ for each value of χ . The arrow in the top-right corner highlights the location

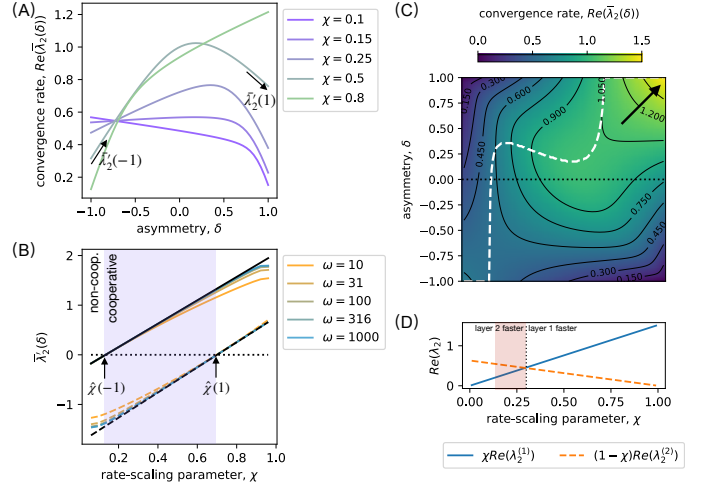


Fig. 5. Combined effects of coupling asymmetry and relative timescale for the second system in Fig. 2(A). (A) We plot the predicted convergence rate $\text{Re}(\bar{\lambda}_2(\delta))$ given by (7)–(9), which assume large coupling strength ω , versus δ for several choices of χ . Black arrows highlight derivative $\bar{\lambda}'_2(\delta) \equiv \frac{d}{d\delta} \text{Re}(\bar{\lambda}_2(\delta))$ for one curve at $\delta = \pm 1$. (B) Black solid and dashed lines indicate our predicted derivatives $\bar{\lambda}'_2(\pm 1)$ given by (12), and colored curves indicate observed values of $\frac{d}{d\delta} \text{Re}(\lambda_2)$ for several choices of ω . As indicated by the shaded region, Rolle's Theorem guarantees the existence of a cooperative optimum when $\chi \in (\hat{\chi}(-1), \hat{\chi}(1))$ [see (14)], where $\hat{\chi}(\pm 1)$ are given by (13) and are the values of χ at which $\bar{\lambda}'_2(\pm 1)$ change sign. (C) We use color to depict $\text{Re}(\bar{\lambda}_2(\delta))$ across the (δ, χ) parameter space. The dashed white curve shows the asymmetry $\hat{\delta}$ that maximizes $\text{Re}(\bar{\lambda}_2(\delta))$ for each value of χ . The arrow in the top-right corner highlights the location of the overall optimum, $\max_{\delta, \chi} \text{Re}(\bar{\lambda}_2(\delta))$, which is a non-cooperative optimum at $(\delta, \chi) \approx (1, 1)$. (D) We plot the convergence rate for each separate layer as a function of χ and highlight a counter-intuitive phenomenon that occurs for the shaded range of χ (see text).

of the overall optimum, $\max_{\delta, \chi} \text{Re}(\bar{\lambda}_2(\delta))$, which is a non-cooperative optimum at $(\delta, \chi) = (1, 1)$. That is, convergence is optimally fast for this system when the first layer is made to be as fast as possible ($\chi = 1$), and it influences the second layer without a reciprocated influence ($\delta = 1$).

In Fig. 5(D), we highlight a counter-intuitive property: when two layers are coupled with an optimal asymmetry parameter $\hat{\delta}$, it may involve the slower system having a greater influence over the faster system. To make this point, the solid blue and dashed orange lines in Fig. 5(D) indicate the separate convergence rate of each (uncoupled) layer. The vertical dotted line in Fig. 5(D) highlights that layer 1 is slower than layer 2 when $\chi < 0.29$. Moreover, observe in Fig. 5(C) that $\hat{\delta} > 0$ (see dashed white curve) for approximately $\chi > 0.13$. Therefore, the shaded region $\chi \in (0.13, 0.29)$ in Fig. 5(D) highlights values of χ in which the optimal asymmetry correspond to when the slower system (layer 1) more strongly influences the faster one (layer 2). That said, our experiments also suggest that if χ is sufficiently large or small (i.e., of one layer is much, much faster than the other), then the optimal asymmetry does coincide with our intuition: the faster system should more strongly influence the slower one.

In Fig. 6, we repeat the experiment shown in Fig. 5, except we now study the six random multiplex networks that were introduced in Sec. 3.3. In Fig. 6(A), we plot

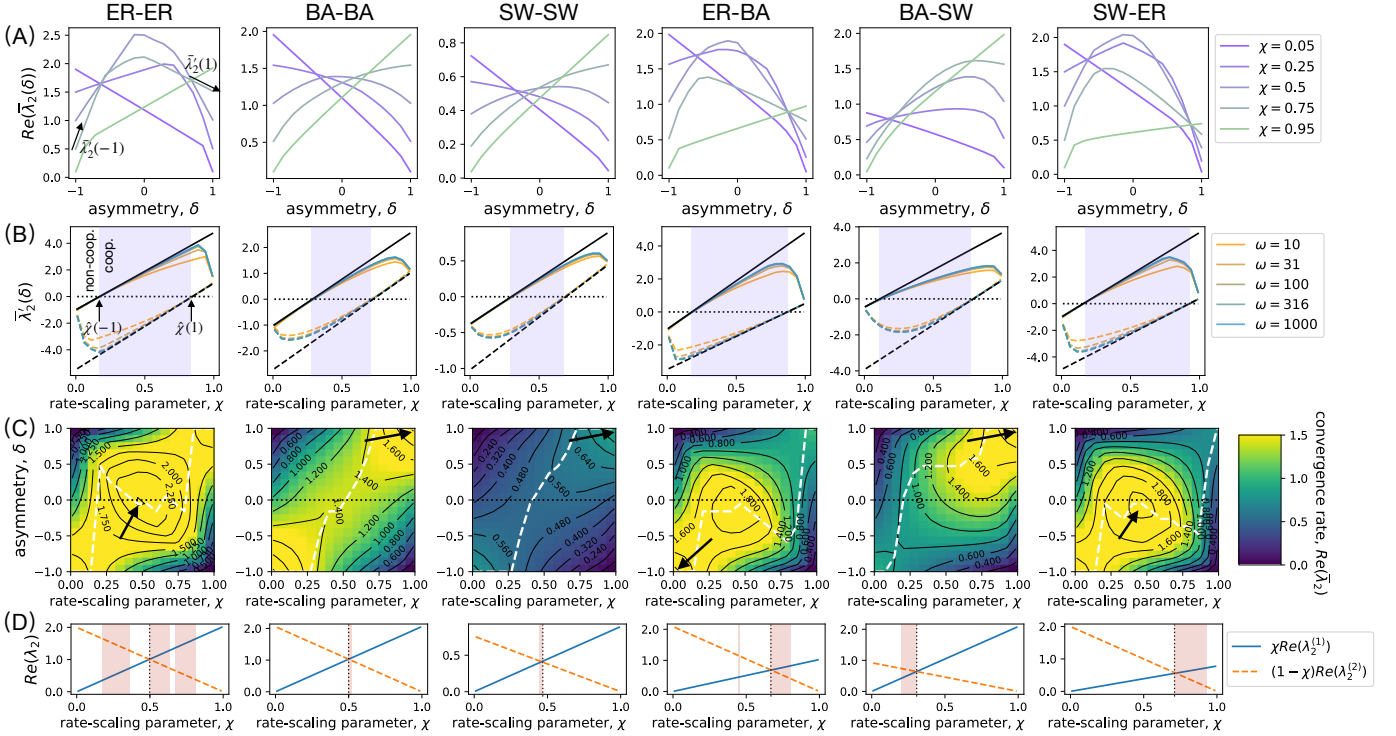


Fig. 6. Combined effects of coupling asymmetry δ and relative timescale χ on the convergence rates for random multiplex networks. Here, we extend the results shown in Fig. 5 to the six random multiplex networks described in Sec. 3.3. The main difference is highlighted by the black arrows in panel (C), which denote the locations of the overall optimum: $\max_{\delta, \chi} \text{Re}(\bar{\lambda}_2(\delta))$. Observe that the overall optimum is cooperative for the ER-ER and SW-ER networks (i.e., see the leftmost and rightmost columns), whereas it is non-cooperative for the others. Additionally, as indicated by the shaded regions in (D), there are several counter-intuitive scenarios. For these value of χ , convergence occurs fastest when the layer with slower dynamics more-strongly influences the faster layer.

$\bar{\lambda}_2(\delta)$ versus δ for several choices of χ , and observe for all networks that the optimum is cooperative when χ is neither too large nor too small. Specifically, this occurs when $\chi \in \{0.25, 0.5, 0.75\}$ for the multiplex networks labeled ER-ER, ER-BA, BA-SW and SW-ER, and when $\chi = 0.5$ for the BA-BA and SW-SW networks. The remaining curves depict a non-cooperative optimum (i.e., layer dominance). These values of χ are in excellent agreement with our predicted ranges of χ that yield a cooperative optimum, which are given by (14) and are indicated by the shaded regions in Fig. 6(B). As before, the solid and dashed black lines illustrate (12).

In Fig. 6(C), we use color to visualize $\text{Re}(\bar{\lambda}_2(\delta))$ across the parameter space $\delta \in [-1, 1]$ and $\chi \in [0, 1]$. In each column, dashed white curves highlight the optimum $\hat{\delta} = \arg\max_{\delta} \text{Re}(\bar{\lambda}_2(\delta))$ for a fixed, given value of χ , whereas the arrows highlight the overall optimum, $\max_{\delta, \chi} \text{Re}(\bar{\lambda}_2(\delta))$. Observe that the overall optimums are cooperative for the models ER-ER and SW-ER, which occur, respectively, near $(\delta, \chi) \approx (-0.1, 0.48)$ and $(\delta, \chi) \approx (-0.03, 0.48)$. Intuitively, consensus is maximally accelerated in both models when the second layer is slightly more influential than the first (i.e., since $\delta < 0$), and the first layers' dynamics are slightly slowed down (i.e., since $\chi < 0.5$). On the other hand, the overall optimum is non-cooperative for the models BA-BA, SW-SW and BA-SW—that is, convergence is optimally fast for these systems when the first layer is made to be as fast as possible ($\chi \rightarrow 1$) and that layer influences the second without reciprocation ($\delta \rightarrow 1$). The model ER-BA also

exhibits a non-cooperative overall optimum; however in this case the optimum involves the second layer dominating the first: $(\delta, \chi) \rightarrow (-1, 0)$.

Finally, lines in Fig. 6(D) illustrate each layers' separate convergence rate, and the shaded regions highlight values of χ in which the dynamics are counter intuitive. For these values of χ , convergence is fastest when the layer with slower dynamics more-strongly influences the faster layer.

5 APPLICATION: MODELING THE COLLECTIVE DECISIONS OF HUMAN-AI SYSTEMS

We propose the interconnected consensus system presented in Sec. 2 as an insightful model for studying the collective decisions of human-AI teams. In Sec. 5.1, we motivate and interpret our model for this application. In Sec. 5.2, we study the network presented in Fig. 1(A), showing that a cooperative optimum requires human-human and AI-AI interactions to have similar timescales. In Sec. 5.3, we study the overall optimum that maximizes the convergences rate by simultaneously tuning layers' timescales and the asymmetry of coupling between the human layer and the AI layer.

5.1 Motivation and Interpretation

Within the social and cognitive sciences, there is a rich literature of dynamical models for collective decision making by social groups and social networks, many of which describe

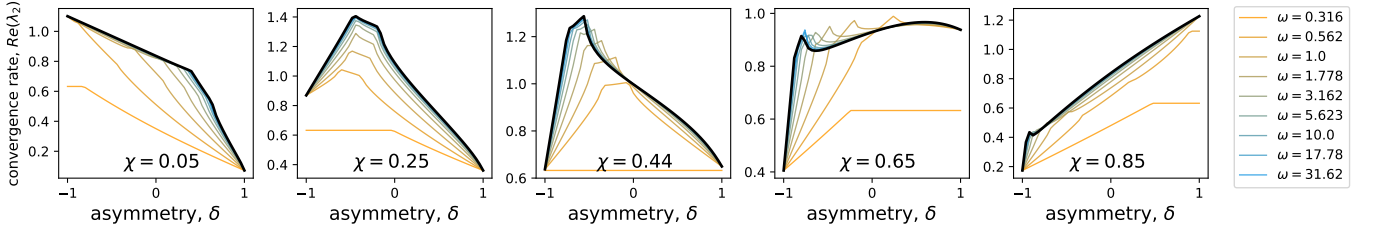


Fig. 7. **A cooperative optimum requires the human and AI network layers have sufficiently similar timescales.** For the system visualized in Fig. 1(A), we plot the convergence rate $\text{Re}(\lambda_2)$ versus δ . Different columns reflect different choices for the rate-scaling parameter $\chi \in (0, 1)$, which tunes whether layer 1 is much faster ($\chi \approx 1$) or layer 2 is much faster ($\chi \approx 0$). Colored curves yield results for different ω (see legend), and black curves depict our theoretical prediction for large ω that is given by (7)–(9). By comparing across the columns, observe that their optima are cooperative for intermediate values of χ (i.e., the second, third and fourth columns) and non-cooperative when χ is either too small or large (see left-most and right-most columns).

processes by which populations can reach consensus [4]–[7]. Of particular interest is the Abelson model [63], [64] for opinion dynamics, which takes the form of a linear differential equation similar to our proposed model (4). Similar consensus models have also been utilized in the biology community to model decision making by animal groups [8], [9] and by the computer science community to implement decentralized algorithms for machine learning and AI [10]–[15]. We offer one interpretation of the latter application—that is, a set of ML/AI models are trained on different data to have different parameter values, and they reach a “collective decision” on the best model parameters using a similar model for consensus.

Given the ubiquity of consensus models for collective decision making in a wide variety of applications, we propose the interconnected consensus system in Sec. 2 as a simple-yet-informative model for collective decisions made by a social network in which individual are supported by AI agents, who themselves coordinate and collectively learn. In this context, the asymmetry parameter has the following interpretation: $\delta > 1$ implies that the humans’ states more strongly influence those of the AI agents, and $\delta < 1$ implies the opposite. Moreover, the rate-scaling parameter χ controls the relative timescale for coordination via human-human interactions as compared to AI-AI interactions. Collective consensus-based decisions within the social network is represented by the intralayer consensus model $\frac{d}{d\tau} \mathbf{x}^{(1)}(\tau) = -\chi \mathbf{L}^{(1)} \mathbf{x}^{(1)}(\tau)$, while consensus among AI agents is represented by $\frac{d}{d\tau} \mathbf{x}^{(2)}(\tau) = -(1 - \chi) \mathbf{L}^{(2)} \mathbf{x}^{(2)}(\tau)$. The choice $\chi \approx 0$ corresponds to when the AI agents coordinate much faster than the humans, while $\chi \approx 1$ implies the opposite.

The two consensus systems are coupled according to (4) so that consensus over the entire system represents a decision that is collectively obtained over the ‘multiplexed’ human-AI social system. Such a model could interpreted as a binary model so that a state $x_p \in \mathbb{R}$ represents the tendency of a human or agent to make some particular binary decision, such as taking a strategic military action [49]–[51] or investing in a particular stock [52]–[54]. Having a strong preference for (or against) such an action would be represented by a large positive (or negative) value, and weaker preferences can be represented by small-magnitude values. We interpret a collective decision of yea or nay as the converged state being positive or negative, and it can

be beneficial for systems to make optimally fast decisions (which can be engineered by maximizing the convergence rate). That said, in real-world scenarios one should also consider other system properties that are essential including, e.g., trust [70] and coordinating agents’ expertise to be complementary [71].

We now further study the multiplex network shown in Fig. 1(A), where layer 1 is an empirical social network that encodes mentoring relationships among corporate executives [62], and as such, our system models a collective business decision in which each executive boardroom member has the unique support of a personalized AI agent. Layer 2 is created as a random directed graph. We will show for this system that the existence of a cooperative versus non-cooperative optimum depends crucially on the relative timescales of two coupled consensus systems. We again focus on the case of $T = 2$ layers with Laplacians given by $\chi \mathbf{L}^{(1)}$ and $(1 - \chi) \mathbf{L}^{(2)}$, where *rate-scaling parameter* $\chi \in (0, 1)$ tunes the relative convergence rate for each layer. We insert these weighted Laplacians into (9) to obtain $\bar{\mathbf{L}}(\delta) = \frac{1+\delta}{2} \chi \mathbf{L}^{(1)} + \frac{1-\delta}{2} (1 - \chi) \mathbf{L}^{(2)}$, and then study how a system’s behavior (i)–(v) depends on both χ and δ . Note that the introduction of χ changes the layers’ separate convergence rates to be $\chi \text{Re}(\lambda_2^{(1)})$ for layer 1 and $(1 - \chi) \text{Re}(\lambda_2^{(2)})$ for layer 2.

5.2 A Cooperative Optimum Requires that Humans and AI-Agents Coordinate on Similar Timescales

We now examine the influence of layers’ relative timescales on the convergence rate for the human-AI system shown in Fig. 1(A). In Fig. 7, we present results for an experiment that is similar to the results shown in Fig. 4. We plot the convergence rate $\text{Re}(\lambda_2)$ versus δ for the human-AI system, and different columns reflect different choices for χ . In each panel, different curves reflect different choices for ω , and black curves indicate our analytical prediction for large ω . By comparing across the columns, observe that their optima are cooperative for intermediate values of χ (i.e., the second, third and fourth columns) and non-cooperative when χ is either too small or large (e.g., see left-most and right-most columns). That is, a cooperative optimum requires that the humans and AI-agents coordinate on similar timescales. Otherwise, we find that the convergence is fastest when the faster layer influences the slower one without a reciprocated influence, i.e., layer dominance.

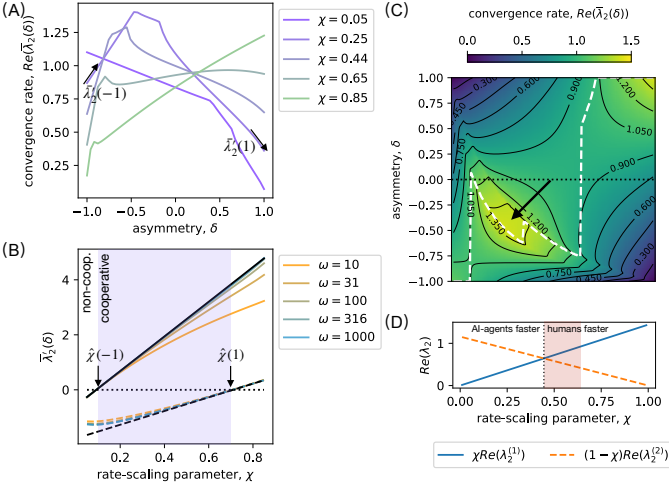


Fig. 8. Combined effects of coupling asymmetry and relative timescale on a Human-AI consensus system. We present identical information as in Fig. 5 but for the Human-AI network that was shown in Fig. 1(A). The main difference is highlighted by the arrow in panel (C): the overall optimum $\max_{\delta, \chi} \text{Re}(\bar{\lambda}_2(\delta))$ is now a cooperative optimum that occurs at approximately $(\delta, \chi) \approx (-0.5, 0.25)$. That is, if one allows coordination within the social-network layer to be faster than that of the AI-agents, or vice versa, and one also allows for asymmetric coupling between these two consensus systems, then for this particular multiplex network, the overall system converges optimally fast when the AI layer coordinates slightly faster than, and has a slightly stronger influence over, the social-network layer.

5.3 Cooperative Optimum Yields Fastest Convergence

In Fig. 8, we present results that are identical to those that were presented in Fig. 5, except we now examine the convergence rate for the human-AI system shown in Fig. 1(A). In Fig. 8(A), we plot $\text{Re}(\bar{\lambda}_2(\delta))$ versus δ for several choices of χ . Observe that the optimum is cooperative for $\chi \in \{0.05, 0.85\}$ and non-cooperative for $\chi \in \{0.25, 0.45, 0.65\}$. This is in agreement with our theory, which is shown Fig. 8(B). Specifically, we find this system to exhibit a cooperative optimum for the approximate range $\chi \in (0.1, 0.7)$ and a non-cooperative optimum outside this range. That is, the rates of AI-AI coordination/communicate should be sufficiently similar to that for human-human coordination/communicate, otherwise the optimally coupled system will be non-cooperative—i.e., convergence will be optimally fast when one network layer influences the other without feedback.

In Fig. 8(C), we plot $\text{Re}(\bar{\lambda}_2(\delta))$ across the parameter space $\delta \in [-1, 1]$ and $\chi \in [0, 1]$. The dashed white curve in indicates the optimum $\delta = \text{argmax}_{\delta} \text{Re}(\bar{\lambda}_2)$ for each value of χ . The black arrow highlights that the overall optimum is cooperative and occurs at the approximate location $(\delta, \chi) \approx (-0.5, 0.25)$. Intuitively, consensus is maximally accelerated when the AI-agents are slightly more influential (i.e., since $\delta < 0$), and collective dynamics among humans are slightly slowed down (i.e., since $\chi < 0.5$).

Finally, in Fig. 8(D), we highlight that an unintuitive property also occurs for this human-AI system. Specifically, the shaded area highlights for the approximate range $\chi \in (0.45, 0.65)$ that convergence is fastest if the slower layer (the AI-agents layer) is actually more influential than the faster layer (the human layer).

Before concluding, we emphasize that these specific findings are a result of the particular network layers that we study (i.e., layer 1 is an empirical social network [62] and we generate layer 2 as a random directed graph). Thus, these network-specific findings describe the behavior of this specific model and should not be simply extrapolated to real-world decision systems. In general, the optimal coupling of a human-AI decisions system will greatly differ from one application to another depending on the specific details of each system, which includes the layers' unique network topologies, their respective dynamics, and one's design goals for that systems. In principle, one should also consider other design factors beyond convergence rate [70], [71]. Nevertheless, our theory provides a baseline of understanding for the effects on convergence rate for human-AI decision systems in which these two network types (a social network and coordinating AI agents) are asymmetrically coupled and have different timescales for collective coordination.

6 DISCUSSION

By now, the scientific literature on multiplex network dynamics is well established [28]. However, most theory focuses on network layers that are symmetrically coupled, and there remains a lack of understanding of how the asymmetric coupling of layers can affect dynamics and also provide new strategies for optimization. This is troubling since real-world networks are often interconnected with one layer being more influential than another. Thus motivated, we formulated a model for multiplex networks in which an asymmetry parameter δ can tune the extent to which interlayer influences are biased in a particular direction. Although our work is primarily motivated by modeling collective behavior over a human-AI system, our formulation of a supraLaplacian $\mathbb{L}(\omega, \delta)$ in (3) using an asymmetry parameter $\delta \in [-1, 1]$ can support the broader study of how coupling asymmetry can affect any Laplacian-related dynamics (i.e., diffusion, synchronization, and so on).

Here, we have focused on the impact of coupling asymmetry on the convergence rate $\text{Re}(\lambda_2)$ toward a collective state, which is an important property that is often optimized for engineered systems [11]–[15]. We provided an initial observation and categorization revealing five distinct ways [see (i)–(v) in Sec. 3.2] in which coupling asymmetry has a nonlinear effect on $\text{Re}(\lambda_2)$. Moreover, it is insightful to consider systems that are optimally coupled and ask whether their coupling is *cooperative*, in that they mutually influence each other, or *non-cooperative*, in that one system directs another without reciprocated feedback. It's worth highlighting that the situation of non-cooperative coupling between network layers closely relates to prior research for collective dynamics over 'master-slave' systems [72]–[74]. These similarities contain subsystems in which one influences another without reciprocated feedback. Our work extends their study to the setting of optimized multiplex networks.

We find a non-cooperative configuration to be optimal when one system is much faster than the other, whereas a cooperative coupling is optimal if the layers have sufficiently similar dynamics timescales. In fact, we obtained

a theoretical criterion (see Sec. 4.2) for when the fastest convergence is cooperative versus non-cooperative. This result, in addition to the system properties (i)–(v) and the structural/dynamical factors influencing (non)-cooperation for optimal systems, should be considered as a stepping stone for further research on the optimization of interconnected systems using techniques that jointly consider coupling asymmetry and timescale tuning. It would be interesting to explore whether our findings/methods are also predictive for more-complicated dynamics including, e.g., the optimization of synchronized chaotic systems [16], [17], [75] and empirical human-AI systems.

See [76] for a codebase that models interconnected consensus systems and reproduces our findings.

ACKNOWLEDGMENTS

The authors would like to thank Sarah Muldoon, Naoki Masuda, and Malbor Asllani for helpful feedback.

REFERENCES

- [1] G. B. Ermentrout, "Review of sync: The emerging science of spontaneous order," *NOTICES OF THE AMS*, vol. 51, no. 3, 2004.
- [2] K. Bansal, J. O. Garcia, S. H. Tompson, T. Verstynen, J. M. Vettel, and S. F. Muldoon, "Cognitive chimera states in human brain networks," *Science advances*, vol. 5, no. 4, p. eaau8535, 2019.
- [3] T. Nishikawa and A. E. Motter, "Comparative analysis of existing models for power-grid synchronization," *New Journal of Physics*, vol. 17, no. 1, p. 015012, 2015.
- [4] V. B. Hinsz, "Cognitive and consensus processes in group recognition memory performance." *Journal of Personality and Social Psychology*, vol. 59, no. 4, p. 705, 1990.
- [5] C. M. Fiol, "Consensus, diversity, and learning in organizations," *Organization Science*, vol. 5, no. 3, pp. 403–420, 1994.
- [6] P. C. Flood, E. Hannan, K. G. Smith, T. Turner, M. A. West, and J. Dawson, "Chief executive leadership style, consensus decision making, and top management team effectiveness," *European Journal of Work and Organizational Psychology*, vol. 9, no. 3, pp. 401–420, 2000.
- [7] S. Mohammed, "Toward an understanding of cognitive consensus in a group decision-making context," *The Journal of Applied Behavioral Science*, vol. 37, no. 4, pp. 408–425, 2001.
- [8] L. Conradt and T. J. Roper, "Consensus decision making in animals," *Trends in Ecology & Evolution*, vol. 20, no. 8, pp. 449–456, 2005.
- [9] P. A. Westley, A. M. Berdahl, C. J. Torney, and D. Biro, "Collective movement in ecology: from emerging technologies to conservation and management," p. 20170004, 2018.
- [10] A. S. Bijral, A. D. Sarwate, and N. Srebro, "Data-dependent convergence for consensus stochastic optimization," *IEEE Transactions on Automatic Control*, vol. 62, no. 9, pp. 4483–4498, 2017.
- [11] M. Assran, N. Loizou, N. Ballas, and M. Rabbat, "Stochastic gradient push for distributed deep learning," in *International Conference on Machine Learning*. PMLR, 2019, pp. 344–353.
- [12] K. Niwa, N. Harada, G. Zhang, and W. B. Kleijn, "Edge-consensus learning: Deep learning on p2p networks with nonhomogeneous data," in *Proceedings of the 26th ACM SIGKDD International Conference on Knowledge Discovery & Data Mining*, 2020, pp. 668–678.
- [13] T. Vogels, S. P. Karimireddy, and M. Jaggi, "Powergossip: Practical low-rank communication compression in decentralized deep learning," *arXiv preprint arXiv:2008.01425*, 2020.
- [14] L. Kong, T. Lin, A. Koloskova, M. Jaggi, and S. U. Stich, "Consensus control for decentralized deep learning," *arXiv preprint arXiv:2102.04828*, 2021.
- [15] B. Huynh, H. Dutta, and D. Taylor, "Impact of community structure on consensus machine learning," *arXiv preprint arXiv:2011.01334*, 2021.
- [16] L. M. Pecora and T. L. Carroll, "Master stability functions for synchronized coupled systems," *Physical review letters*, vol. 80, no. 10, p. 2109, 1998.
- [17] J. Sun, E. M. Bollt, and T. Nishikawa, "Master stability functions for coupled nearly identical dynamical systems," *EPL (Europhysics Letters)*, vol. 85, no. 6, p. 60011, 2009.
- [18] P. S. Skardal, D. Taylor, and J. Sun, "Optimal synchronization of complex networks," *Physical review letters*, vol. 113, no. 14, p. 144101, 2014.
- [19] D. Taylor, P. S. Skardal, and J. Sun, "Synchronization of heterogeneous oscillators under network modifications: Perturbation and optimization of the synchrony alignment function," *SIAM journal on applied mathematics*, vol. 76, no. 5, pp. 1984–2008, 2016.
- [20] A. Y. Kibangou, "Graph laplacian based matrix design for finite-time distributed average consensus," in *2012 American Control Conference (ACC)*. IEEE, 2012, pp. 1901–1906.
- [21] J.-C. Delvenne, S. N. Yaliraki, and M. Barahona, "Stability of graph communities across time scales," *Proceedings of the national academy of sciences*, vol. 107, no. 29, pp. 12755–12760, 2010.
- [22] S. Boyd, P. Diaconis, and L. Xiao, "Fastest mixing markov chain on a graph," *SIAM review*, vol. 46, no. 4, pp. 667–689, 2004.
- [23] N. Masuda, M. A. Porter, and R. Lambiotte, "Random walks and diffusion on networks," *Physics Reports*, vol. 716–717, pp. 1–58, 2017. [Online]. Available: <http://www.sciencedirect.com/science/article/pii/S0370157317302946>
- [24] R. R. Coifman and M. Maggioni, "Diffusion wavelets," *Applied and computational harmonic analysis*, vol. 21, no. 1, pp. 53–94, 2006.
- [25] P. G. Doyle and J. L. Snell, *Random walks and electric networks*. American Mathematical Soc., 1984, vol. 22.
- [26] M. Kivelä, A. Arenas, M. Barthelemy, J. P. Gleeson, Y. Moreno, and M. A. Porter, "Multilayer networks," *Journal of Complex Networks*, vol. 2, no. 3, pp. 203–271, 2014.
- [27] S. Boccaletti, G. Bianconi, R. Criado, C. Del Genio, J. Gómez-Gardeñes, M. Romance, I. Sendina-Nadal, Z. Wang, and M. Zanin, "The structure and dynamics of multilayer networks," *Physics Reports*, vol. 544, no. 1, pp. 1–122, 2014.
- [28] E. Cozzo, G. F. De Arruda, F. A. Rodrigues, and Y. Moreno, *Multiplex Networks: Basic Formalism and Structural Properties*. Springer, 2018.
- [29] P. J. Mucha, T. Richardson, K. Macon, M. A. Porter, and J.-P. Onnela, "Community structure in time-dependent, multiscale, and multiplex networks," *Science*, vol. 328, no. 5980, pp. 876–878, May 2010.
- [30] A. Solé-Ribalta, M. De Domenico, S. Gómez, and A. Arenas, "Random walk centrality in interconnected multilayer networks," *Physica D*, vol. 323, pp. 73–79, 2016.
- [31] C. Ding and K. Li, "Centrality ranking in multiplex networks using topologically biased random walks," *Neurocomputing*, vol. 312, pp. 263–275, 2018. [Online]. Available: <http://www.sciencedirect.com/science/article/pii/S0925231218307069>
- [32] D. Taylor, "Multiplex markov chains: Convection cycles and optimality," *Physical Review Research*, vol. 2, no. 3, p. 033164, 2020.
- [33] J. Aguirre, R. Sevilla-Escoboza, R. Gutiérrez, D. Papo, and J. M. Buldú, "Synchronization of interconnected networks: the role of connector nodes," *Physical Review Letters*, vol. 112, no. 24, p. 248701, 2014.
- [34] L. V. Gambuzza, M. Frasca, and J. Gomez-Gardenes, "Intra-layer synchronization in multiplex networks," *EPL (Europhysics Letters)*, vol. 110, no. 2, p. 20010, 2015.
- [35] S. Jalan and A. Singh, "Cluster synchronization in multiplex networks," *EPL (Europhysics Letters)*, vol. 113, no. 3, p. 30002, 2016.
- [36] J. Sawicki, I. Omelchenko, A. Zakharova, and E. Schöll, "Delay controls chimera relay synchronization in multiplex networks," *Physical Review E*, vol. 98, no. 6, p. 062224, 2018.
- [37] H. Liu, J. Li, Z. Li, Z. Zeng, and J. Lü, "Intralayer synchronization of multiplex dynamical networks via pinning impulsive control," *IEEE Transactions on Cybernetics*, 2020.
- [38] S. Gómez, A. Díaz-Guilera, J. Gómez-Gardeñes, C. J. Pérez-Vicente, Y. Moreno, and A. Arenas, "Diffusion dynamics on multiplex networks," *Physical Review Letters*, vol. 110, no. 2, p. 028701, 2013.
- [39] A. Solé-Ribalta, M. De Domenico, N. E. Kouvaris, A. Diaz-Guilera, S. Gomez, and A. Arenas, "Spectral properties of the laplacian of multiplex networks," *Physical Review E*, vol. 88, no. 3, p. 032807, 2013.
- [40] D. R. DeFord and S. D. Pauls, "A new framework for dynamical models on multiplex networks," *Journal of Complex Networks*, vol. 6, no. 3, pp. 353–381, 2018.

- [41] J. Bragard, S. Boccaletti, and H. Mancini, "Asymmetric coupling effects in the synchronization of spatially extended chaotic systems," *Physical review letters*, vol. 91, no. 6, p. 064103, 2003.
- [42] M. Timme, "Does dynamics reflect topology in directed networks?" *EPL (Europhysics Letters)*, vol. 76, no. 3, p. 367, 2006.
- [43] J. G. Restrepo and E. Ott, "Mean-field theory of assortative networks of phase oscillators," *EPL (Europhysics Letters)*, vol. 107, no. 6, p. 60006, 2014.
- [44] P. S. Skardal, D. Taylor, J. Sun, and A. Arenas, "Erosion of synchronization in networks of coupled oscillators," *Physical Review E*, vol. 91, no. 1, p. 010802(R), 2015.
- [45] T. Nishikawa and A. E. Motter, "Symmetric states requiring system asymmetry," *Physical Review Letters*, vol. 117, no. 11, p. 114101, 2016.
- [46] M. Asllani, R. Lambiotte, and T. Carletti, "Structure and dynamical behavior of non-normal networks," *Science Advances*, vol. 4, no. 12, p. eaau9403, 2018.
- [47] F. Molnar, T. Nishikawa, and A. E. Motter, "Asymmetry underlies stability in power grids," *Nature communications*, vol. 12, no. 1, pp. 1–9, 2021.
- [48] D. Taylor, P. S. Skardal, and J. Sun, "Introduction to focus issue: Symmetry and optimization in the synchronization and collective behavior of complex systems," *Chaos*, no. 30, p. 060401, 2020.
- [49] R. Rasch, A. Kott, and K. D. Forbus, "Incorporating ai into military decision making: an experiment," *IEEE Intelligent Systems*, vol. 18, no. 4, pp. 18–26, 2003.
- [50] X. Zhou, W. Wang, T. Wang, Y. Lei, and F. Zhong, "Bayesian reinforcement learning for multi-robot decentralized patrolling in uncertain environments," *IEEE Transactions on Vehicular Technology*, vol. 68, no. 12, pp. 11 691–11 703, 2019.
- [51] A. T. Azar, A. Koubaa, N. Ali Mohamed, H. A. Ibrahim, Z. F. Ibrahim, M. Kazim, A. Ammar, B. Benjdira, A. M. Khamis, I. A. Hameed *et al.*, "Drone deep reinforcement learning: A review," *Electronics*, vol. 10, no. 9, p. 999, 2021.
- [52] A. Albadvi, S. K. Chaharsooghi, and A. Esfahanipour, "Decision making in stock trading: An application of promethee," *European journal of operational research*, vol. 177, no. 2, pp. 673–683, 2007.
- [53] L. Yu, K. K. Lai, and S. Wang, "Designing a hybrid ai system as a forex trading decision support tool," in *17th IEEE International Conference on Tools with Artificial Intelligence (ICTAI'05)*. IEEE, 2005, pp. 5–pp.
- [54] S.-c. T. Chou, H.-j. Hsu, C.-c. Yang, and F. Lai, "A stock selection dss combining ai and technical analysis," *Annals of Operations Research*, vol. 75, pp. 335–353, 1997.
- [55] A. Tejedor, A. Longjas, E. Foufoula-Georgiou, T. T. Georgiou, and Y. Moreno, "Diffusion dynamics and optimal coupling in multiplex networks with directed layers," *Physical Review X*, vol. 8, no. 3, p. 031071, 2018.
- [56] X. Wang, A. Tejedor, Y. Moreno *et al.*, "Unique superdiffusion induced by directionality in multiplex networks," *New Journal of Physics*, 2021.
- [57] J. Kunegis, S. Schmidt, A. Lommatzsch, J. Lerner, E. W. De Luca, and S. Albayrak, "Spectral analysis of signed graphs for clustering, prediction and visualization," in *Proceedings of the 2010 SIAM international conference on data mining*. SIAM, 2010, pp. 559–570.
- [58] L. Pan, H. Shao, and M. Mesbahi, "Laplacian dynamics on signed networks," in *2016 IEEE 55th Conference on decision and control (CDC)*. IEEE, 2016, pp. 891–896.
- [59] D. Taylor, S. A. Myers, A. Clauset, M. A. Porter, and P. J. Mucha, "Eigenvector-based centrality measures for temporal networks," *Multiscale Modeling & Simulation*, vol. 15, no. 1, pp. 537–574, 2017.
- [60] D. Taylor, M. A. Porter, and P. J. Mucha, "Tunable eigenvector-based centralities for multiplex and temporal networks," *Multiscale Modeling & Simulation*, vol. 15, no. 1, pp. 537–574, 2021.
- [61] G. Cencetti and F. Battiston, "Diffusive behavior of multiplex networks," *New Journal of Physics*, vol. 21, no. 3, p. 035006, 2019.
- [62] D. Krackhardt, "Cognitive social structures," *Social Networks*, vol. 9, no. 2, pp. 109–134, 1987.
- [63] R. P. Abelson, "Mathematical models of the distribution of attitudes under controversy," *Contributions to mathematical psychology*, 1964.
- [64] —, "Mathematical models in social psychology," in *Advances in experimental social psychology*. Elsevier, 1967, vol. 3, pp. 1–54.
- [65] M. Domenico, "Datasets released for reproducibility; available at <https://manliodomenico.com/data.php>."
- [66] P. ERDdS and A. R&wi, "On random graphs i," *Publ. math. debrecen*, vol. 6, no. 290–297, p. 18, 1959.
- [67] A.-L. Barabási and R. Albert, "Emergence of scaling in random networks," *science*, vol. 286, no. 5439, pp. 509–512, 1999.
- [68] D. J. Watts and S. H. Strogatz, "Collective dynamics of 'small-world' networks," *nature*, vol. 393, no. 6684, pp. 440–442, 1998.
- [69] P. Sahoo and T. Riedel, *Mean Value Theorems and Functional Equations*. World Scientific, 1998.
- [70] N. Ezer, S. Bruni, Y. Cai, S. J. Hepenstal, C. A. Miller, and D. D. Schmorow, "Trust engineering for human-ai teams," in *Proceedings of the Human Factors and Ergonomics Society Annual Meeting*, vol. 63, no. 1. SAGE Publications Sage CA: Los Angeles, CA, 2019, pp. 322–326.
- [71] G. Bansal, B. Nushi, E. Kamar, W. S. Lasecki, D. S. Weld, and E. Horvitz, "Beyond accuracy: The role of mental models in human-ai team performance," in *Proceedings of the AAAI Conference on Human Computation and Crowdsourcing*, vol. 7, 2019, pp. 2–11.
- [72] H. Haken, "Synergetics," *Physics Bulletin*, vol. 28, no. 9, p. 412, 1977.
- [73] J. Suykens, P. Curran, and L. Chua, "Master-slave synchronization using dynamic output feedback," *International Journal of Bifurcation and Chaos*, vol. 7, no. 03, pp. 671–679, 1997.
- [74] J. Pena Ramirez, A. Arellano-Delgado, and H. Nijmeijer, "Enhancing master-slave synchronization: The effect of using a dynamic coupling," *Physical Review E*, vol. 98, no. 1, p. 012208, 2018.
- [75] P. S. Skardal, R. Sevilla-Escoboza, V. Vera-Ávila, and J. M. Buldú, "Optimal phase synchronization in networks of phase-coherent chaotic oscillators," *Chaos: An Interdisciplinary Journal of Nonlinear Science*, vol. 27, no. 1, p. 013111, 2017.
- [76] Z. Song, "Code release: Interconnected consensus systems with asymmetric coupling; available at https://github.com/zhaos426/Interconnected_Consensus_Systems_with_Asymmetric_Coupling."



Zhao Song received a B.S. degree in Information and Computing Science from Henan University of Technology, China, in 2015. and the M.A. and Ph.D. degrees in Mathematics from the University at Buffalo, the State University of New York, USA, in 2018 and 2021. She is currently working as a research associate at the Department of Mathematics, Dartmouth College, USA. Her research focuses on multiplex networks and network dynamics in network science.



Dane Taylor received a PhD in applied mathematics from the University of Colorado, Boulder in 2013. Before joining the University of Wyoming in 2023, Dr. Taylor held positions at the Statistical and Applied Mathematical Sciences Institute (2013-2015), the University of North Carolina at Chapel Hill (2015-2017), and the University at Buffalo, SUNY (2017-2023). Dr. Taylor has published over 35 papers on network modeling for data science and dynamical systems and has been the main organizer for events including the Northeast Regional Conference on Complex Systems (NERCCS) and the SIAM Workshop on Network Science.

APPENDIX A FURTHER STUDY OF NONROBUST OPTIMA

Here, we further investigate $\text{Re}(\lambda_2)$ for the multiplex network shown in the center column of Fig. 2(A). In the center column of Fig. 2(B), we plotted $\text{Re}(\lambda_2)$ versus δ for these interconnected consensus systems and observed two optima near $\delta = \pm 0.35$. We classify these as “nonrobust” optima, because the derivative $\frac{d}{d\delta}\text{Re}(\lambda_2)$ is undefined (i.e., discontinuous) at these optima.

Here, we show that these two nonrobust optima (and the lack of differentiability) arise due to a spectral bifurcation in which the two eigenvalues λ_2 and λ_3 of $\mathbb{L}(\omega, \delta)$ collide and give rise to a complex pair of eigenvalues. Here, we have defined λ_2 and λ_3 as the eigenvalues of $\mathbb{L}(\omega, \delta)$ with second-smallest and third-smallest real part, respectively.

In Fig. 9, we plot λ_2 and λ_3 for a supraLaplacian $\mathbb{L}(\omega, \delta)$ associated with $\omega = 30$ and various δ for the system shown in the center column of Fig. 2(A). In panels (A) and (B) of Fig. 9, we depict the real and imaginary parts, respectively, of these eigenvalues. Symbols indicate observed values that are directly computed using $\mathbb{L}(\omega, \delta)$, whereas solid and dashed black curves indicate theoretical predictions that we will present in the next section. Note that the observed and predicted eigenvalues are in excellent agreement.

Observe in Fig. 9(A) that the theoretical curve for λ_2 is identical to the one that is in the center column of Fig. 2(B). The curve has two optima near $\delta \pm 0.35$, and these values coincide with spectral bifurcations in which λ_2 and λ_3 change from being distinct real-valued eigenvalues to being a complex pair of eigenvalues (or vice versa). That is, for $|\delta| \leq 0.35$, the eigenvalues λ_2 and λ_3 are purely real (i.e., $\text{Im}(\lambda_2) = \text{Im}(\lambda_3) = 0$ and $\text{Re}(\lambda_3) > \text{Re}(\lambda_2)$). In contrast, for $|\delta| > 0.35$, the eigenvalues λ_2 and λ_3 are complex numbers and $\text{Re}(\lambda_3) = \text{Re}(\lambda_2)$. Thus, the nonrobust optima at $\delta = \pm 0.35$ arise for these interconnected consensus systems because of a spectral bifurcation.

In Fig. 10, we present a information that is identical to what we presented in Figs. 5 and 8, except that we now consider the multiplex network shown in the center column of Fig. 2(A). In Fig. 10 (A), we plot $\text{Re}(\bar{\lambda}_2(\delta))$ versus δ

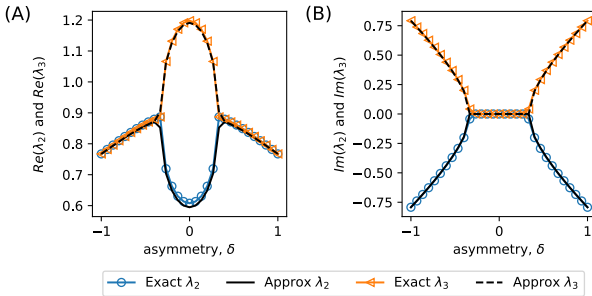


Fig. 9. A collision between eigenvalues λ_2 and λ_3 yields a spectral bifurcation and nonrobust optima. We plot (A) the real parts and (B) imaginary parts of λ_2 and λ_3 versus δ for the interconnected consensus systems shown in the center column of Fig. 2(A). Symbols depict observed eigenvalues that are directly computed using $\mathbb{L}(\omega, \delta)$ with $\omega = 30$, whereas black curves are theoretical predictions. The nonrobust optima at $\delta = \pm 0.35$ coincide with a spectral bifurcation in which λ_2 and λ_3 collide to yield a complex pair of eigenvalues.

for several choices of χ . Observe for $\chi = 0.49$ that there exist two nonrobust optima because of spectral bifurcations, which we explained in Fig. 9. This is the only value of χ that we examine for which our theory guarantees cooperative optimum, and in fact, a non-cooperative optimum can be observed for the other values $\chi \in \{0.05, 0.27, 0.72, 0.95\}$. Specifically, we depict our theory from Section 4.2 in Fig. 10 (B), and the shaded $\chi \in (0.39, 0.6)$ indicates the values of χ for which a cooperative optimum is guaranteed.

In Fig. 10 (C), we visualize $\text{Re}(\bar{\lambda}_2(\delta))$ for the parameter space $\delta \in [-1, 1]$ and $\chi \in [0, 1]$. As before, the dashed white curve indicates the optimum $\hat{\delta} = \text{argmax}_\delta \text{Re}(\bar{\lambda}_2)$ asymmetry for each value of χ . The black arrow highlights that the overall optimum occurs approximately when either $(\delta, \chi) = (-1, 0)$ or $(\delta, \chi) = (1, 1)$. That is, the overall optimum only occurs when one layer is set to be as fast as possible and it non-cooperatively influences the other layer. Due to symmetry, it doesn’t matter which layer is chosen to be the dominator.

In Fig. 10 (D), solid blue and dashed orange lines indicate the separate convergence rate of each (uncoupled) system: $\chi \text{Re}(\lambda_2^{(1)})$ for system 1 and $(1 - \chi) \text{Re}(\lambda_2^{(2)})$ for system 2. Note for $\chi > 0.5$ that layer 1 is the faster system, and vice versa for $\chi < 0.5$. Compare this to the dashed white curve in Fig. 10 (C), where one can observe that $\hat{\delta} < 0$ for $\chi < 0.5$ and $\hat{\delta} > 0$ for $\chi > 0.5$. Therefore, for this system, it is always optimal for the faster layer to more strongly influence the slower layer. See Figs. 5 (D) and 8 (D) for counter-intuitive situations in which the convergence is fastest when the slower system more-strongly influences the faster one.

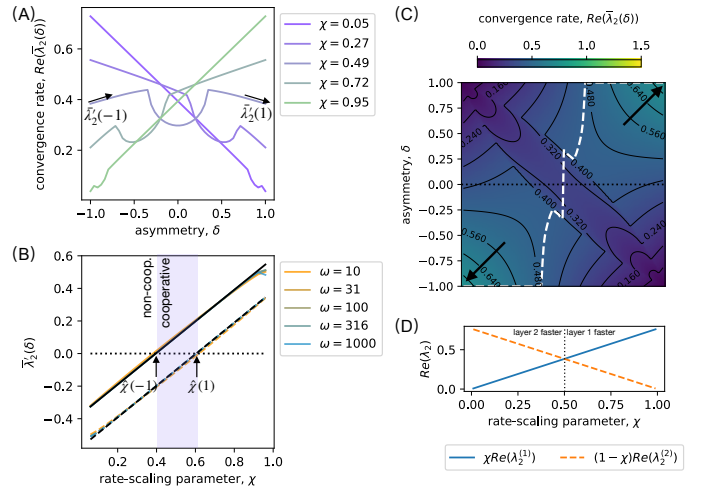


Fig. 10. Combined effects of coupling asymmetry and relative timescale on the third system in Fig. 2(A). We present identical information as in Figs. 4 and 5 but for the multiplex network that was visualized in the third column of Fig. 2. The main difference here can be seen in panels (C) and (D). The two arrows in (C) highlight that there are now two overall optimal choices for δ and χ (both are non-cooperative), and the lack of a shaded region in (D) highlights that there is no counter-intuitive phenomenon whereby it is optimal for the slower system to more strongly influence the faster one.

APPENDIX B

DERIVATION OF EQUATIONS (7)–(9)

Here, we provide our derivation of (7) and (8), which predict the eigenvalue $\lambda_2(\omega, \delta)$ of $\mathbb{L}(\omega, \delta)$ in the limit of large ω . We do not have ω and δ in the main paper, but will keep these parameters in the appendix. We will use perturbation theory for directed multiplex networks that is similar to that which was developed in [32], [60].

First, we introduce a change of variables $\epsilon = 1/\omega$ and multiply both sides of (3) by ϵ to obtain

$$\tilde{\mathbb{L}}(\epsilon, \delta) = \epsilon \mathbb{L}(\epsilon^{-1}, \delta) = \epsilon \mathbb{L}^I + \mathbb{L}^I(\delta). \quad (\text{B.1})$$

Because we've only scaled the matrix $\mathbb{L}(\omega, \delta)$ by ϵ , it follows that $\tilde{\lambda}_2(\epsilon, \delta) = \epsilon \lambda_2$ is an eigenvalue of $\tilde{\mathbb{L}}(\epsilon, \delta)$. Let $\mathbf{u}(\epsilon, \delta)$ and $\mathbf{v}(\epsilon, \delta)$ be the associated left and right eigenvectors of $\tilde{\mathbb{L}}(\epsilon, \delta)$. Note that scalar multiplication does not change the eigenvectors of a matrix, and so $\mathbf{u}(\epsilon, \delta)$ and $\mathbf{v}(\epsilon, \delta)$ are also the eigenvectors of $\mathbb{L}(\omega, \delta)$ that are associated with λ_2 . The main motivation for this transformation is that we can more easily study λ_2 in $\omega \rightarrow \infty$ limit by instead studying $\tilde{\lambda}_2(\epsilon, \delta)$ as $\epsilon \rightarrow 0^+$. In this limit,

$$\tilde{\mathbb{L}}(\epsilon, \delta) \rightarrow \mathbb{L}^I(\delta) = \mathbf{L}^I(\delta) \otimes \mathbf{I}. \quad (\text{B.2})$$

To proceed, we first establish some properties about the eigenvalues and eigenvectors of $\mathbf{L}^I(\delta) \otimes \mathbf{I}$.

Lemma B.1. *Let μ be an eigenvalue of $\mathbf{L}^I(\delta) \in \mathbb{R}^{T \times T}$ and \mathbf{u} and \mathbf{v} , respectively, be its associated left and right eigenvectors. Furthermore, let $\mathbf{e}^{(i)} \in \mathbb{R}^N$ denote the i -th unit vector such that all entries are zeros, except for entry i , which is a one. It then follows that μ is an eigenvalue of $\mathbf{L}^I(\delta) \otimes \mathbf{I}$, and it has associated left and right eigenvectors given by*

$$\tilde{\mathbf{u}}^{(i)} = \mathbb{P}(\mathbf{e}^{(i)} \otimes \mathbf{u}), \quad \tilde{\mathbf{v}}^{(i)} = \mathbb{P}(\mathbf{e}^{(i)} \otimes \mathbf{v}), \quad (\text{B.3})$$

where \mathbb{P} is a “stride permutation matrix” that contains entries

$$P_{ij} = \begin{cases} 1, & j = \lceil i/N \rceil + T[(i-1) \bmod N] \\ 0, & \text{otherwise.} \end{cases}$$

Remark B.1.1. *As discussed in [59], [60], this stride permutation is a unitary matrix that changes the ordering of indices for a supramatrix associated with a multiplex network. That is, the indices originally count by nodes and then layers, but after applying \mathbb{P} , the counting is first by layers and then by nodes.*

Remark B.1.2. *Lemma B.1 is true for any choice $i \in \{1, \dots, N\}$, and so each eigenvalue μ of $\mathbf{L}^I(\delta) \otimes \mathbf{I}$ has an eigenspace that is at least N -dimensional. [It may be larger if μ is a repeated eigenvalue of $\mathbf{L}^I(\delta)$.]*

Proof. The stride permutation yields an identity

$$\mathbf{L}^I(\delta) \otimes \mathbf{I} = \mathbb{P}(\mathbf{I} \otimes \mathbf{L}^I(\delta))\mathbb{P}^T, \quad (\text{B.4})$$

where

$$\mathbf{I} \otimes \mathbf{L}^I(\delta) = \begin{pmatrix} \mathbf{L}^I(\delta) & 0 & \cdots & 0 \\ 0 & \mathbf{L}^I(\delta) & \cdots & 0 \\ \vdots & \vdots & \ddots & \vdots \\ 0 & 0 & \cdots & \mathbf{L}^I(\delta) \end{pmatrix}. \quad (\text{B.5})$$

Since \mathbb{P} is a unitary matrix, the eigenvalues of $\mathbf{L}^I(\delta) \otimes \mathbf{I}$ are identical to those of $\mathbf{I} \otimes \mathbf{L}^I(\delta)$. Moreover, if \mathbf{v} is a right

eigenvector of $\mathbf{I} \otimes \mathbf{L}^I(\delta)$ with eigenvalue μ_2 , then $\mathbb{P}\mathbf{v}$ is a right eigenvector of $\mathbf{L}^I(\delta) \otimes \mathbf{I}$. This can easily be checked:

$$\begin{aligned} (\mathbf{L}^I(\delta) \otimes \mathbf{I})\mathbb{P}\mathbf{v} &= \mathbb{P}(\mathbf{I} \otimes \mathbf{L}^I(\delta))\mathbb{P}^T\mathbb{P}\mathbf{v} \\ &= \mathbb{P}(\mathbf{I} \otimes \mathbf{L}^I(\delta))\mathbf{v} \\ &= \mu\mathbb{P}\mathbf{v}. \end{aligned} \quad (\text{B.6})$$

One can similarly show that if \mathbf{u} is a left eigenvector for $\mathbf{I} \otimes \mathbf{L}^I(\delta)$, then $\mathbb{P}\mathbf{u}$ is one for $\mathbf{L}^I(\delta) \otimes \mathbf{I}$. What remains for us to show is that $\mathbf{u} = \mathbf{e}^{(i)} \otimes \mathbf{u}$ and $\mathbf{v} = \mathbf{e}^{(i)} \otimes \mathbf{v}$ are left and right eigenvectors of $\mathbf{I} \otimes \mathbf{L}^I(\delta)$. We prove this using a standard property for the product of two Kronecker products:

$$\begin{aligned} (\mathbf{I} \otimes \mathbf{L}^I(\delta))(\mathbf{e}^{(i)} \otimes \mathbf{v}) &= (\mathbf{I}\mathbf{e}^{(i)}) \otimes (\mathbf{L}^I(\delta)\mathbf{v}) \\ &= \mathbf{e}^{(i)} \otimes \mu\mathbf{v} \\ &= \mu(\mathbf{e}^{(i)} \otimes \mathbf{v}). \end{aligned} \quad (\text{B.7})$$

A similar result can be obtained for the left eigenvector $\mathbf{e}^{(i)} \otimes \mathbf{u}$. \square

Having established basic results for the spectral properties of $\mathbf{L}^I(\delta) \otimes \mathbf{I}$ in Lemma B.1, we are now ready to study the eigenvalue $\tilde{\lambda}_2(\epsilon, \delta)$ of $\tilde{\mathbb{L}}(\epsilon, \delta)$ that has the second-smallest real part in the limit $\epsilon \rightarrow 0^+$. We formalize this result with in following theorem.

Theorem B.2. *Assume that a supraLaplacian $\mathbb{L}(\omega, \delta)$ corresponds to a strongly connected graph. Further, let $\mathbf{u}(\delta) = [u_1(\delta), \dots, u_T(\delta)]^T$ be the left eigenvector of an interlayer Laplacian $\mathbf{L}^I(\delta)$ that is associated with the zero-valued (i.e., trivial) eigenvalue. Then the eigenvalue $\lambda_2(\omega, \delta)$ of $\mathbb{L}(\omega, \delta)$ that has second-smallest real part has the following limit:*

$$\lim_{\omega \rightarrow \infty} \lambda_2(\omega, \delta) = \bar{\lambda}_2(\delta), \quad (\text{B.8})$$

where $\bar{\lambda}_2(\delta)$ is the eigenvalue of matrix

$$\bar{\mathbf{L}}(\delta) = \sum_{t=1}^T w_t(\delta) \mathbf{L}^t(\delta) \quad (\text{B.9})$$

that has the second-smallest real part, and $w_t(\delta) = u_t(\delta) / \sum_{t'} u_{t'}(\delta)$.

Proof. Consider first-order Taylor expansions for the eigenvalue $\tilde{\lambda}_2(\epsilon, \delta)$ of $\tilde{\mathbb{L}}(\epsilon, \delta)$ and its associated left and right eigenvectors:

$$\tilde{\lambda}_2(\epsilon, \delta) = \tilde{\lambda}_2(0, \delta) + \epsilon \tilde{\lambda}'_2(0, \delta) + \mathcal{O}(\epsilon^2), \quad (\text{B.10a})$$

$$\tilde{\mathbf{u}}(\epsilon, \delta) = \tilde{\mathbf{u}}(0, \delta) + \epsilon \tilde{\mathbf{u}}'(0, \delta) + \mathcal{O}(\epsilon^2), \quad (\text{B.10b})$$

$$\tilde{\mathbf{v}}(\epsilon, \delta) = \tilde{\mathbf{v}}(0, \delta) + \epsilon \tilde{\mathbf{v}}'(0, \delta) + \mathcal{O}(\epsilon^2). \quad (\text{B.10c})$$

Note that we have defined the derivatives

$$\tilde{\lambda}'_2(\epsilon, \delta) \equiv \frac{d}{d\epsilon} \tilde{\lambda}_2(\epsilon, \delta), \quad (\text{B.11a})$$

$$\tilde{\mathbf{u}}'(\epsilon, \delta) \equiv \frac{d}{d\epsilon} \tilde{\mathbf{u}}(\epsilon, \delta), \quad (\text{B.11b})$$

$$\tilde{\mathbf{v}}'(\epsilon, \delta) \equiv \frac{d}{d\epsilon} \tilde{\mathbf{v}}(\epsilon, \delta). \quad (\text{B.11c})$$

We first consider the term $\tilde{\lambda}_2(0, \delta)$. Since we assumed $\mathbf{L}^I(\delta)$ to be the Laplacian of a strongly connected graph, the smallest eigenvalue $\mu_1 = 0$ of $\mathbf{L}^I(\delta)$ is guaranteed to be a simple eigenvalue with multiplicity 1. Lemma B.1 implies

$\mu_1 = 0$ is an eigenvalue of $\mathbf{L}^I(\delta) \otimes \mathbf{I}$ with an N -dimensional eigenspace. Hence, matrix $\tilde{\mathbf{L}}(\epsilon, \delta)$ has N eigenvalues that converge to 0 as $\epsilon \rightarrow 0^+$ (and in fact, one of these eigenvalues is always exactly equal to zero). By definition (i.e., since it has the smallest, positive real part), the eigenvalue $\tilde{\lambda}_2(\epsilon, \delta)$ of $\tilde{\mathbf{L}}(\epsilon, \delta)$ must be one of these eigenvalues, which implies that $\tilde{\lambda}_2(0, \delta) = 0$.

Next, we consider the derivative term $\tilde{\lambda}'_2(0, \delta)$. We will show that it equals the second smallest eigenvalue of the matrix defined in (8). To this end, we consider the eigenvalue equation

$$\tilde{\mathbf{L}}(\epsilon, \delta) \tilde{\mathbf{v}}(\epsilon, \delta) = \tilde{\lambda}_2(\epsilon, \delta) \tilde{\mathbf{v}}(\epsilon, \delta), \quad (\text{B.12})$$

and we expand all terms to first order to obtain

$$\begin{aligned} & \left[\epsilon \mathbb{L}^L + \mathbb{L}^I(\delta) \right] \left[\tilde{\mathbf{v}}(0, \delta) + \epsilon \tilde{\mathbf{v}}'(0, \delta) \right] \\ & = \left[\tilde{\lambda}_2(0, \delta) + \epsilon \tilde{\lambda}'_2(0, \delta) \right] \left[\tilde{\mathbf{v}}(0, \delta) + \epsilon \tilde{\mathbf{v}}'(0, \delta) \right]. \end{aligned} \quad (\text{B.13})$$

The zeroth-order and first-order terms must be consistent, which gives rise to two separate equations. The equation associated with the zeroth-order terms yields an eigenvalue equation

$$\mathbb{L}^I(\delta) \tilde{\mathbf{v}}(0, \delta) = \tilde{\lambda}_2(0, \delta) \tilde{\mathbf{v}}(0, \delta). \quad (\text{B.14})$$

Lemma B.1 implies that the eigenvalue $\tilde{\lambda}_2(0, \delta) = 0$ has an N -dimensional right eigenspace spanned by right eigenvectors having the form $\tilde{\mathbf{v}}^{(i)} = \mathbb{P}(\mathbf{e}^{(i)} \otimes \mathbf{v})$ for $i \in \{1, 2, \dots, N\}$. We similarly define $\tilde{\mathbf{u}}^{(i)} = \mathbb{P}(\mathbf{e}^{(i)} \otimes \mathbf{u})$ for the left eigenspace. Note that the vectors \mathbf{u} and \mathbf{v} contain entries that are nonnegative, which can be proved using the Perron–Frobenius theorem.

Next, we expand $\tilde{\mathbf{v}}(0, \delta)$ in this eigenbasis as

$$\tilde{\mathbf{v}}(0, \delta) = \sum_i \tilde{\alpha}_i \tilde{\mathbf{v}}^{(i)}. \quad (\text{B.15})$$

We define a vector of coordinates $\tilde{\boldsymbol{\alpha}} = [\tilde{\alpha}_1, \dots, \tilde{\alpha}_N]^T$ that must be determined, and we note that the vector must be normalized with $\|\tilde{\boldsymbol{\alpha}}\|_2 = 1$.

The first-order terms in (B.13) give rise to a linear equation

$$\mathbb{L}^L \tilde{\mathbf{v}}(0, \delta) + \mathbb{L}^I(\delta) \tilde{\mathbf{v}}'(0, \delta) = \tilde{\lambda}'_2(0, \delta) \tilde{\mathbf{v}}(0, \delta), \quad (\text{B.16})$$

which has used that $\tilde{\lambda}_2(0, \delta) = 0$.

To solve for $\tilde{\lambda}'_2(0, \delta)$, we left multiply by a left eigenvector $\tilde{\mathbf{u}}^{(i')} = \mathbb{P}(\mathbf{e}^{(i')} \otimes \mathbf{u})$ of $\mathbb{L}^I(\delta)$ and again use $\tilde{\lambda}_2(0, \delta) = 0$ to obtain

$$\left[\tilde{\mathbf{u}}^{(i')} \right]^* \mathbb{L}^L \tilde{\mathbf{v}}(0, \delta) = \tilde{\lambda}'_2(0, \delta) \left[\tilde{\mathbf{u}}^{(i')} \right]^* \tilde{\mathbf{v}}(0, \delta), \quad (\text{B.17})$$

where $\left[\tilde{\mathbf{u}}^{(i')} \right]^*$ denotes the conjugate transpose of vector $\tilde{\mathbf{u}}^{(i')}$. Using the general form of $\tilde{\mathbf{v}}(0, \delta)$ from (B.15), we obtain

$$\sum_{i=1}^N \tilde{\alpha}_i \left[\tilde{\mathbf{u}}^{(i')} \right]^* \mathbb{L}^L \tilde{\mathbf{v}}^{(i)} = \tilde{\lambda}'_2(0, \delta) \sum_{i=1}^N \tilde{\alpha}_i \left[\tilde{\mathbf{u}}^{(i')} \right]^* \tilde{\mathbf{v}}^{(i)}. \quad (\text{B.18})$$

This system is identical to the following eigenvalue equation $\bar{\mathbf{L}}(\delta) \tilde{\boldsymbol{\alpha}} = \tilde{\lambda}'_2(0, \delta) \tilde{\boldsymbol{\alpha}}$, where

$$\bar{\mathbf{L}}(\delta)_{i'i} = \frac{\left[\tilde{\mathbf{u}}^{(i')} \right]^* \mathbb{L}^L \tilde{\mathbf{v}}^{(i)}}{\left[\tilde{\mathbf{u}}^{(i')} \right]^* \tilde{\mathbf{v}}^{(i)}}, \quad (\text{B.19})$$

$\tilde{\boldsymbol{\alpha}} = [\tilde{\alpha}_1, \dots, \tilde{\alpha}_N]^T$, and $\tilde{\lambda}'_2(0, \delta) = \bar{\lambda}_2(\delta)$ is the eigenvalue with second-smallest real part. We can further simplify this result using the definitions of $\tilde{\mathbf{u}}^{(i')} = \mathbb{P}(\mathbf{e}^{(i')} \otimes \mathbf{u})$ and $\tilde{\mathbf{v}}^{(i)} = \mathbb{P}(\mathbf{e}^{(i)} \otimes \mathbf{v})$ to obtain

$$\bar{\mathbf{L}}(\delta)_{i'i} = \frac{[\mathbf{u}]^* \mathbf{L}^{(i',i)} \mathbf{v}}{[\mathbf{u}]^* \mathbf{v}} = \sum_{t=1}^T \left(\frac{u_t}{\sum_t u_t} \right) L_{i'i}^{(t)}, \quad (\text{B.20})$$

where

$$\mathbf{L}^{(i',i)} = \text{diag} \left(L_{i'i}^{(1)}, L_{i'i}^{(2)}, \dots, L_{i'i}^{(T)} \right), \quad (\text{B.21})$$

and $L_{i'i}^{(t)}$ denotes the (i', i) -component of intralayer Laplacian $\mathbf{L}^{(t)}$. (B.20) follows after using the definition of \mathbb{P} , which is a unitary matrix that permutes the enumeration of nodes and layers as described for Lemma B.1. (B.21) follows after using that the right eigenvector \mathbf{v} that is associated with the zero eigenvalue is spanned by the all-ones vector, $\mathbf{v} \propto [1, \dots, 1]^T$. Finally, we recall that $\epsilon = 1/\omega$ and $\epsilon \lambda_2(\omega, \delta) = \tilde{\lambda}_2(0, \delta) + \epsilon \tilde{\lambda}'_2(0, \delta) + \mathcal{O}(\epsilon^2)$, which implies

$$\lim_{\omega \rightarrow \infty} \lambda_2(\omega, \delta) = \lim_{\epsilon \rightarrow 0^+} \left[0 + \tilde{\lambda}'_2(0, \delta) + \mathcal{O}(\epsilon) \right] = \bar{\lambda}_2(\delta). \quad (\text{B.22})$$

□

Corollary B.3. *Let $\mathbf{L}^{(1)}$ and $\mathbf{L}^{(2)}$ be the intralayer Laplacians of a two-layer multiplex network. The weighted-average Laplacian $\bar{\mathbf{L}}(\delta)$ given in (8) can be simplified as*

$$\bar{\mathbf{L}}(\delta) = \left(\frac{1 + \delta}{2} \right) \mathbf{L}^{(1)} + \left(\frac{1 - \delta}{2} \right) \mathbf{L}^{(2)}. \quad (\text{B.23})$$

Proof. The interlayer Laplacian for $T = 2$ asymmetrically coupled layers is given by (2), and its zero-valued eigenvalue has left eigenvector $\mathbf{u}(\delta) = [1 + \delta, 1 - \delta]^T$. The result follows after using that $u_1(\delta) = 1 + \delta$, $u_2(\delta) = 1 - \delta$, and $u_1(\delta) + u_2(\delta) = 2$. □

APPENDIX C

DERIVATION OF EQUATIONS (12) AND (13)

Lemma C.1. *Let $\mathbf{L}^{(1)}$ and $\mathbf{L}^{(2)}$ be the intralayer Laplacians of a two-layer multiplex network, and define $\chi \in (0, 1]$ to be a time-scaling parameter that varies the relative timescale of dynamics for the two layers through the mapping: $\mathbf{L}^{(1)} \mapsto \chi \mathbf{L}^{(1)}$ and $\mathbf{L}^{(2)} \mapsto (1 - \chi) \mathbf{L}^{(2)}$. (Note that the dynamics of layer 1 is much faster as $\chi \rightarrow 1$, whereas layer 2 is much faster as $\chi \rightarrow 0$.) Further, let $\bar{\mathbf{L}}(\delta)$ be the weighted-average Laplacian given in (9) under this mapping. It then follows that*

$$\bar{\mathbf{L}}(\delta) = \frac{1 + \delta}{2} \chi \mathbf{L}^{(1)} + \frac{1 - \delta}{2} (1 - \chi) \mathbf{L}^{(2)}. \quad (\text{C.1})$$

Theorem C.2. *Let $\bar{\lambda}'_2(\delta) \equiv \frac{d}{d\delta} \text{Re}(\bar{\lambda}_2(\delta))$ be the derivative of the real part of $\bar{\lambda}_2(\delta)$ who is the second-smallest eigenvalue of the weighted-average Laplacian $\bar{\mathbf{L}}(\delta)$. Further, let $\mathbf{u}^{(2)}$ and $\mathbf{v}^{(2)}$ be the left and right eigenvectors for the second smallest eigenvalue*

$\lambda_2^{(t)}$ of intralayer Laplacian $\mathbf{L}^{(t)}$ for $t \in \{1, 2\}$, assuming $\lambda_2^{(t)}$ is simple. We then find the following limits as $\delta \rightarrow \pm 1$

$$\begin{aligned} \bar{\lambda}_2'(1) &= \text{Re} \left(\frac{-\mathbf{u}^{(1)*} \mathbf{L}^{(2)} \mathbf{v}^{(1)}}{2\mathbf{u}^{(1)*} \mathbf{v}^{(1)}} \right) \\ &\quad + \chi \text{Re} \left(\frac{\mathbf{u}^{(1)*} (\mathbf{L}^{(1)} + \mathbf{L}^{(2)}) \mathbf{v}^{(1)}}{2\mathbf{u}^{(1)*} \mathbf{v}^{(1)}} \right), \end{aligned} \quad (\text{C.2a})$$

$$\begin{aligned} \bar{\lambda}_2'(-1) &= \text{Re} \left(\frac{-\lambda_2^{(2)}}{2} \right) \\ &\quad + \chi \text{Re} \left(\frac{\mathbf{u}^{(2)*} (\mathbf{L}^{(1)} + \mathbf{L}^{(2)}) \mathbf{v}^{(2)}}{2\mathbf{u}^{(2)*} \mathbf{v}^{(2)}} \right), \end{aligned} \quad (\text{C.2b})$$

where \mathbf{u}^* denotes the conjugate transpose of vector \mathbf{u} .

Proof. We first consider $\delta \rightarrow -1$ and note the identity

$$\begin{aligned} &\frac{1+\delta}{2} \chi \mathbf{L}^{(1)} + \frac{1-\delta}{2} (1-\chi) \mathbf{L}^{(2)} \\ &= (1-\chi) \mathbf{L}^{(2)} + (1+\delta) \frac{\chi \mathbf{L}^{(1)} - (1-\chi) \mathbf{L}^{(2)}}{2} \\ &= (1-\chi) \mathbf{L}^{(2)} + (1+\delta) \chi \frac{\mathbf{L}^{(1)} + \mathbf{L}^{(2)}}{2} - (1+\delta) \frac{\mathbf{L}^{(2)}}{2}. \end{aligned} \quad (\text{C.3})$$

We Taylor expand the eigenvalue $\bar{\lambda}_2(\delta)$ and its associated left and right eigenvectors $\bar{\mathbf{u}}(\delta)$ and $\bar{\mathbf{v}}(\delta)$, respectively, to find

$$\bar{\lambda}_2(\delta) = \bar{\lambda}_2(-1) + (1+\delta) \bar{\lambda}_2'(-1) + \mathcal{O}((1+\delta)^2), \quad (\text{C.4a})$$

$$\bar{\mathbf{u}}(\delta) = \bar{\mathbf{u}}(-1) + (1+\delta) \bar{\mathbf{u}}'(-1) + \mathcal{O}((1+\delta)^2), \quad (\text{C.4b})$$

$$\bar{\mathbf{v}}(\delta) = \bar{\mathbf{v}}(-1) + (1+\delta) \bar{\mathbf{v}}'(-1) + \mathcal{O}((1+\delta)^2). \quad (\text{C.4c})$$

We substitute the first-order approximations into the eigenvalue equation $\bar{\mathbf{L}}(\delta) \bar{\mathbf{v}}(\delta) = \bar{\lambda}_2(\delta) \bar{\mathbf{v}}(\delta)$ to obtain

$$\begin{aligned} &\left[\frac{1+\delta}{2} \chi \mathbf{L}^{(1)} + \frac{1-\delta}{2} (1-\chi) \mathbf{L}^{(2)} \right] \left[\bar{\mathbf{v}}(-1) + (1+\delta) \bar{\mathbf{v}}'(-1) \right] \\ &= \left[\bar{\lambda}_2(-1) (1+\delta) \bar{\lambda}_2'(-1) \right] \left[\bar{\mathbf{v}}(-1) + (1+\delta) \bar{\mathbf{v}}'(-1) \right]. \end{aligned} \quad (\text{C.5})$$

The zeroth-order and first-order terms must both be consistent, which gives rise to two equations. The zeroth-order terms yield an eigenvalue equation

$$(1-\chi) \mathbf{L}^{(2)} \bar{\mathbf{v}}(-1) = \bar{\lambda}_2(-1) \bar{\mathbf{v}}(-1), \quad (\text{C.6})$$

which implies that $\bar{\mathbf{v}}(-1) = \mathbf{v}^{(2)}$ and $\bar{\lambda}_2(-1) = (1-\chi) \lambda_2^{(2)}$. The first-order terms yield a linear equation

$$\begin{aligned} &(1-\chi) \mathbf{L}^{(2)} \bar{\mathbf{v}}'(-1) + \frac{\chi \mathbf{L}^{(1)} - (1-\chi) \mathbf{L}^{(2)}}{2} \mathbf{v}^{(2)} \\ &= (1-\chi) \lambda_2^{(2)} \bar{\mathbf{v}}'(-1) + \bar{\lambda}_2'(-1) \mathbf{v}^{(2)}. \end{aligned} \quad (\text{C.7})$$

We left multiply both sides of this equation by $\mathbf{u}^{(2)*}$ to obtain

$$\chi \text{Re} \left(\frac{\mathbf{u}^{(2)*} (\mathbf{L}^{(1)} + \mathbf{L}^{(2)}) \mathbf{v}^{(2)}}{2\mathbf{u}^{(2)*} \mathbf{v}^{(2)}} \right) - \text{Re} \left(\frac{\lambda_2^{(2)}}{2} \right) = \bar{\lambda}_2'(-1). \quad (\text{C.8})$$

This complete the analysis for $\delta \rightarrow -1$. We repeat this procedure for $\delta \rightarrow 1$ to complete the proof. \square

Theorem C.3. Consider the following two roots for the linear equations defined in (C.2a),

$$\hat{\chi}(1) = \text{Re} \left(\frac{\mathbf{u}^{(1)*} \mathbf{L}^{(2)} \mathbf{v}^{(1)}}{\mathbf{u}^{(1)*} (\mathbf{L}^{(1)} + \mathbf{L}^{(2)}) \mathbf{v}^{(1)}} \right), \quad (\text{C.9a})$$

$$\hat{\chi}(-1) = \text{Re} \left(\frac{\mathbf{u}^{(2)*} \mathbf{L}^{(2)} \mathbf{v}^{(2)}}{\mathbf{u}^{(2)*} (\mathbf{L}^{(1)} + \mathbf{L}^{(2)}) \mathbf{v}^{(2)}} \right), \quad (\text{C.9b})$$

and also define

$$s_1 = \text{Re} \left(\frac{\mathbf{u}^{(1)*} (\mathbf{L}^{(1)} + \mathbf{L}^{(2)}) \mathbf{v}^{(1)}}{\mathbf{u}^{(1)*} \mathbf{v}^{(1)}} \right), \quad (\text{C.10a})$$

$$s_2 = \text{Re} \left(\frac{\mathbf{u}^{(2)*} (\mathbf{L}^{(1)} + \mathbf{L}^{(2)}) \mathbf{v}^{(2)}}{\mathbf{u}^{(2)*} \mathbf{v}^{(2)}} \right). \quad (\text{C.10b})$$

Under the assumption that s_1 and s_2 are both positive, and $\hat{\chi}(-1), \hat{\chi}(1) \in [0, 1]$ with $\hat{\chi}(-1) < \hat{\chi}(1)$, then the convergence rate $\text{Re}(\bar{\lambda}_2(\delta))$ for a 2-layer multiplex network is guaranteed to have a cooperative maximum at some value $\delta \in (-1, 1)$ if $\chi \in (\hat{\chi}(-1), \hat{\chi}(1))$.

Proof. Our proof relies on Rolle's Theorem [69] for a continuous function $f(\delta)$ on some domain $\delta \in [a, b]$: if $f'(a) > 0$ and $f'(b) < 0$, then there exists at least one value of $\hat{\delta}$ at which the function $f(\delta)$ obtains its maximum. In our case, $f(\delta) = \text{Re}(\bar{\lambda}_2(\delta))$ and $[a, b] = [-1, 1]$. Thus, the maximum is guaranteed to exist provided that $\bar{\lambda}_2'(-1) > 0$ and $\bar{\lambda}_2'(1) < 0$.

This criterion can be generally checked for any δ by simply evaluating $\bar{\lambda}_2'(\delta)$ at $\delta = \pm 1$. Moreover, we can apply these bounds on the right-hand-sides of (12) and solve for χ to obtain intervals within which an optimum is guaranteed. Depending on the different signs that s_1 and s_2 can take and the values of $\hat{\chi}(-1)$ and $\hat{\chi}(1)$, in principle, different types of intervals are possible. In the simplest case, both s_1 and s_2 are positive and the Rolle's Theorem inequalities are equivalent to the inequalities $\chi > \hat{\chi}(-1)$ and $\chi < \hat{\chi}(1)$. Also, assuming that $0 \leq \hat{\chi}(-1) < \hat{\chi}(1) \leq 1$, then we can conclude that a cooperative maximum exists when $\chi \in (\hat{\chi}(-1), \hat{\chi}(1))$. \square

APPENDIX D

EXTENDED STUDY OF OPTIMA FOR RANDOM MULTIPLEX NETWORKS

Here, we further study the effects of layers' relative timescales on optima for the family of random multiplex networks described in Sec. 3.3 in which each layer is created using one of three models: the Erdős-Rényi (ER) model [66], Barabási-Albert (BA) model [67], or the Watts-Strogatz small-world (SW) model [68]. The main extension here is that we now consider many different choices for these generative models.

In Fig. 11, we plot our theoretically predicted convergence rate $\text{Re}(\bar{\lambda}_2(\delta))$ given by (7)–(9) versus δ . Different columns reflect different choices for the rate-scaling parameter χ , and different rows correspond to different generative

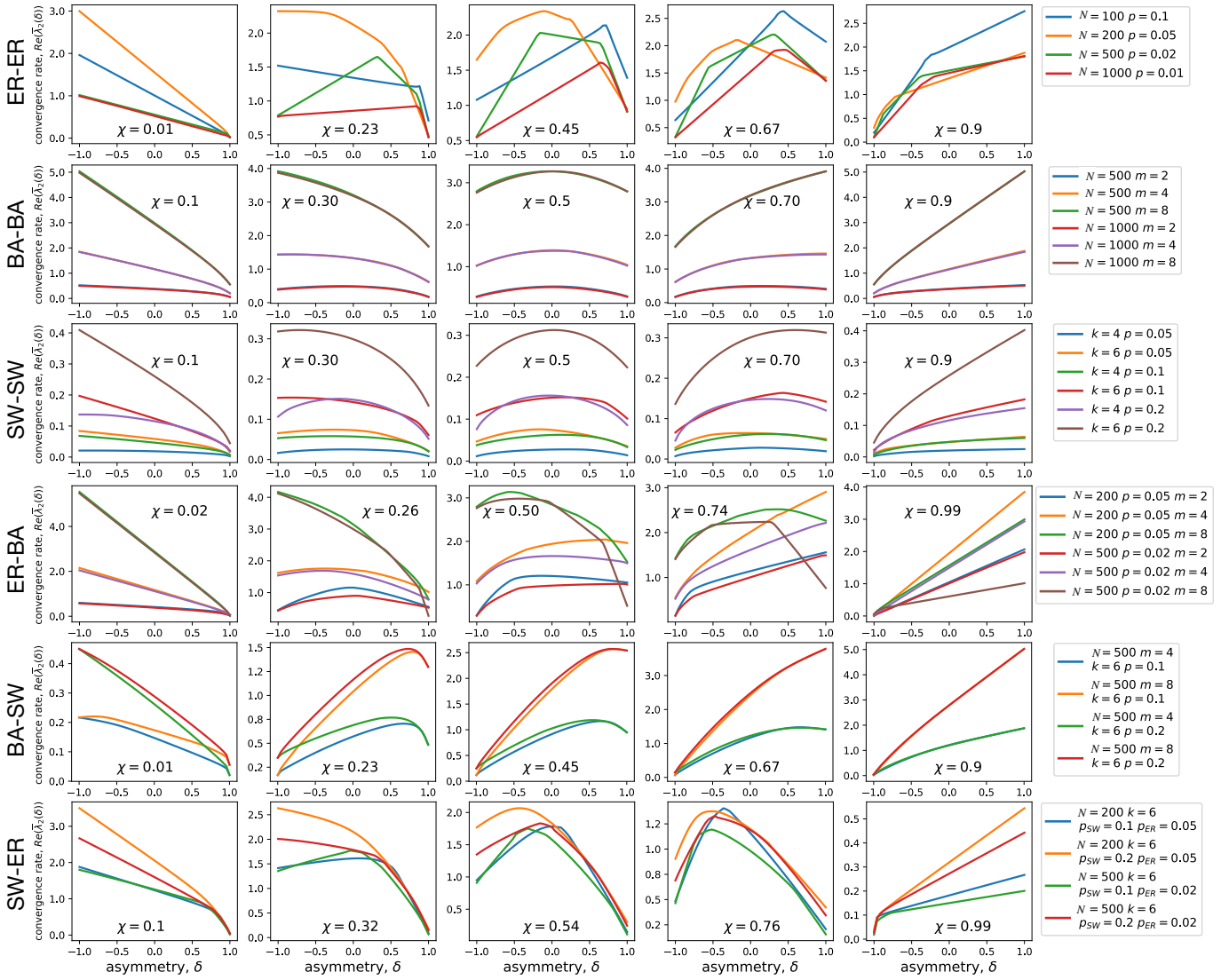


Fig. 11. Layers’ relative timescales influence whether optima are cooperative vs. non-cooperative for random multiplex networks. We plot our theoretical prediction given by (7)–(9)) for the convergence rate versus δ . The six rows show $\text{Re}(\lambda_2(\delta))$ for the six random multiplex networks introduced in Sec. 3.3, and the different curves reflect different parameter choices for the random-graph layers (see legend). The different columns correspond to different choices for the rate-scaling parameter $\chi \in (0, 1)$, which tunes whether layer 1 is much faster ($\chi \approx 1$) or layer 2 is much faster ($\chi \approx 0$). In all cases, we find that the optima are cooperative for intermediate values of χ (e.g., third column) and non-cooperative when χ is either too small or large (e.g., left-most and right-most columns).

processes for the random multiplex networks. For example, “ER-BA” indicates that layer 1 is created as an ER random graph, while layer 2 is created by the Barabási-Albert (BA) preferential-attachment model. In each panel, the colored curves depict various parameter choices for the random-graph models (see legends). By comparing across the columns, observe that their optima are cooperative for intermediate values of χ (e.g., the third column) and non-cooperative when χ is either too small or large (e.g., the left-most and right-most columns).

By focusing on the second and fourth columns in Fig. 11, one can observe that some curves yield a cooperative optimum while others do not, depending the parameter choices for the generative models. This allows us to study how network parameters affect $\text{Re}(\lambda_2)$ and whether the optimum is cooperative vs. non-cooperative. For example, consider ER-BA model in the fourth row, for which we

study six parameter-choice combinations. For the first three parameter choices (blue, orange and green curves), we fix the number $N = 200$ of nodes and the probability $p = 0.05$ for edge creation, and vary the constant m used for the BA model. For the last three parameter choices, we consider the same three values of m but decrease p to $p = 0.02$. Our first observation is these changes in m appear to have a greater effect than the change to p . Also, observe in the second column (i.e., $\chi = 0.26$) that increasing m can change the optimum from non-cooperative to cooperative for both choices of p . Interesting, the opposite can be observed in the fourth column (i.e., $\chi = 0.74$); increasing m changes the optimum from non-cooperative to cooperative. Given this complicated response, we leave open to future research further investigations into the diverse effects of network parameter choices on $\text{Re}(\lambda_2)$ for random multiplex networks.